Nonrigid Image Registration Using Physically Based Models

by

Zhao Yi

A thesis
presented to the University of Waterloo
in fulfilment of the
thesis requirement for the degree of
Master of Mathematics
in
Computer Science

Waterloo, Ontario, Canada, 2006

I hereby declare that I am the sole author of this thesis.

I authorize the University of Waterloo to lend this thesis to other institutions or individuals for the purpose of scholarly research.

I further authorize the University of Waterloo to reproduce this thesis by photocopying or by other means, in total or in part, at the request of other institutions or individuals for the purpose of scholarly research.

Abstract

It is well known that biological structures such as human brains, although may contain the same global structures, differ in shape, orientation, and fine structures across individuals and at different times. Such variabilities during registration are usually represented by nonrigid transformations. This research seeks to address this issue by developing physically based models in which transformations are constructed to obey certain physical laws.

In this thesis, a novel registration technique is presented based on the physical behavior of particles. Regarding the image as a particle system without mutual interaction, we simulate the registration process by a set of free particles moving toward the target positions under applied forces. The resulting partial differential equations are a nonlinear hyperbolic system whose solution describes the spatial transformation between the images to be registered. They can be numerically solved using finite difference methods.

This technique extends existing physically based models by completely excluding mutual interaction and highly localizing image deformations. We demonstrate its performance on a variety of images including two-dimensional and three-dimensional, synthetic and clinical data. Deformable images are achieved with sharper edges and clearer texture at less computational cost.

Acknowledgments

First and foremost, I wish to express my heartfelt thanks to my supervisor Justin Wan, for his constant guidance in my research field, invaluable help during my master's study, significant training in academic writing, and excellent teaching in critical thinking.

My deep appreciation also goes to other members of my reading committee, Jeff Orchard and Edward Vrscay. Their warmly encouragement, constructive comments, and untiring assistance have been of great value during the preparation of this thesis.

I am grateful to Hany Farid, who kindly provided me the experimental data that I regard as so important.

Last, but not the least, I would like to thank my family and friends. Thanks to my parents, my boyfriend Yue for their ceaseless love and support. Thanks to my colleagues in Scientific Computation Group for providing a stimulating and fun environment in which to learn and grow.

Contents

List of Figures

List of Tables

Chapter 1

Introduction

It is very common to utilize imaging as a tool in modern medicine. The presence of medical images provides clear, detailed visual information about a specific part of the body that may not be externally visible. It helps doctors thoroughly study the regions of interest and thus leads to improved medical treatment. Very often, multiple images are acquired from various sources for clinical purpose. To easily relate different information displayed in separate images, we geometrically align relevant images to share a common coordinate system. This process is known as image registration.

Considerable attention has been received on this problem over the last decades. Contributing researchers come from different backgrounds (e.g., physicians, electrical engineers, computer scientists, applied mathematicians) with distinct emphasis. Our focus in particular is nonrigid registration, where the spatial relationship between images is not limited to rotation and translation only. For example, when inspecting images of a soft tissue, we need to take into account its deformation effect. The vast variabilities allowed during nonrigid registration substantially broaden its applicability; however, it also raises major difficulties in finding image correspondence. Therefore, nonrigid registration is still an active research subject which presents unique challenges as well as interesting applications.

Numerous algorithms have been developed in this area; however, more accurate and efficient methods are still needed. Some registration techniques parameterize

the spatial transformation by a geometric model with low degrees of freedom. The optimal values of the parameters are often determined by prescribed correspondence between labeled landmarks. A simple example is the widely used affine transformation model [26] extended from rigid registration. If basis functions such as splines [4] and wavelets [1] are introduced into geometric modeling, higher degrees of freedom can also be achieved. The main advantage of these techniques is that the obtained transformations can be stated in analytical form which leads to efficient computation. However, the limited degrees of freedom may not be adequate for complicated registration problems. An alternative approach is to adopt physically based models in which transformations are constructed to obey certain physical laws. Pioneered by Bajcsy [2], elastic registration techniques model the registration process by the deformation of an elastic solid. Assuming linear elasticity, they are restricted to small linear deformations. To overcome this drawback, fluid registration techniques [10] are proposed in which the registration process is modeled by the flow of a viscous fluid. They can allow relatively larger deformations; however, the inherent viscosity may introduce a smearing artifact to the deformed image. An improvement has been made by introducing an extra elastic term to bound the fluid viscosity, which leads to viscoelastic registration techniques [40].

To avoid blurring resulting from fluid viscosity, we propose to use an inviscid model. Instead of regarding the image as a fluid continuum with viscous interaction, we simulate the deformation process as a set of free particles moving toward the target positions under applied forces. To observe the movement of particles, Lagrangian reference frame is often used. But it needs to track individual particles and is hard to apply. Assuming there are enough particles moving around, we can fit Eulerian reference frame to the particle framework. A novel registration technique is thus developed based on the physical behavior of particles. The resulting partial differential equations are a nonlinear hyperbolic system whose solution describes the spatial transformation between the images to be registered. They can be numerically solved using finite difference methods.

The particle registration technique is quite simple and efficient. Since it can be viewed as an inviscid fluid model, the smearing artifact caused by the viscous terms is eliminated and large deformations can be accommodated. Also, because

of its simplicity in simulation, total computational cost is decreased. Thus, the particle registration technique can achieve a deformed image with more contrast and sharper edges in less time. We have successfully applied the particle model to medical image datasets yielding fast and accurate registrations.

The rest of this thesis is organized as follows. Chapter 2 contains an overview of image registration problems. A general description is given, including different registration classification and various medical applications. In addition, we mathematically formulate image registration into an optimization problem where the objective function consists of a similarity measure and a regularization term. Chapter 3 introduces physically based models for nonrigid registration. A physical analog is established to model the registration process by related physical principles. The elastic models, fluid models, and viscoelastic models are described. Chapter 4 presents an inviscid registration technique expressed in a particle framework. We derive the governing equations from particle dynamics, and interpret particle registration into the variational form. To control the desired transformation, a regularity constraint is imposed over the registration process. Chapter 5 discusses numerical implementation details for solving the objective PDE system, including discretization methods, stability conditions, regridding procedure, and multiresolution scheme. Chapter 6 shows experimental results on 2D and 3D, synthetic and real datasets, with various validation techniques used to evaluate the accuracy and efficiency. Finally, conclusions are drawn in Chapter 7, where we briefly review the physical modeling, summarize its key features, and suggest some possible improvements in the future. The background knowledge of continuum mechanics is presented in the Appendix.

Chapter 2

Image Registration Problems

Image registration requires aligning an image pair with an optimal transformation. It has many potential applications in the clinic, and is an often encountered problem in various research fields. We begin the chapter with a general description of image registration problems, the registration classification, and its medical applications. We also present a mathematical formulation of how image registration is defined and interpreted as an optimization problem consisting of a similarity measure and a regularization term.

2.1 General Description

Medical images result from sensors for the purpose of visualizing a specific part of the body that is not externally visible. To characterize the detected properties, a certain quantity, usually intensity, must apply. The mapping of detected properties to intensity values is determined by the physics of the particular sensor acquiring images and the chosen imaging parameters during acquisition.

Various sensors are used to acquire medical images, consequently numerous modalities exist nowadays. Each modality provides unique information of the area being imaged. For example, anatomical modalities, including magnetic resonance imaging (MRI), x-rays, computed tomography (CT), ultrasound, etc., provide anatomical information such as geometric shapes and relative positions of

structures. On the other hand, functional modalities, including positron emission tomography (PET), single photo emission computed tomography (SPECT), functional magnetic resonance imaging (fMRI), etc., provide functional information such as activity maps and dynamic regions of organs. Different sensors generally generate different modalities, however, images of the same modality may not have the same intensity maps due to different imaging parameters.

The problem of registration arises, for instance, when two images need to be compared for diagnosis. It is defined as the process of finding a spatial transformation that best aligns the image pair under consideration. The inputs are two images to be registered, the output is a spatial transformation which maps points in one image to points in another image.

Each registration task is unique and can be described by the feature of the input images, including dimensionality, modality, subject, and object. The dimensionality of the given images may be two or three, which leads to two dimensional, three dimensional, or multidimensional registration. If the images to be registered are of the same modality, monomodal registration is performed. Otherwise, registration between different modalities is called multimodal registration. When the image pair involves a single patient, we call it intrasubject registration. As a counterpart, intersubject registration is accomplished using two images of different patients. Additionally, atlas registration takes place between patients and atlases. The object of registration refers to the particular region of anatomy to be registered. It varies from head, brain, to liver, vertebra.

2.1.1 Classification

Various registration methods exist, and they can be classified in different ways [23]. Here we only focus on three aspects, i.e., registration basis, domain of transformation, and transformation type.

Registration basis refers to the kind of image features used to derive the registration. Based on the nature of registration basis, we can classify registration into landmark based and intensity based methods.

Landmark based registration first extracts landmarks from given images, i.e., geometric features like points [14], curves [12], surfaces [34], objects [19], and then computes a transformation based on these landmarks. Often, a preprocessing of labeling and segmentation is required before registration can be performed. Alternatively, intensity based registration directly exploits the image intensities to compute the transformation (e.g., [2, 15, 33]). The main advantage is that an explicit preprocessing of the images is not required. However, it generally requires a higher computational cost and a stronger dependence on image modality and imaging parameters.

Domain of transformation refers to the image area on which the transformation can be applied. Basically there are two kinds of transformation domain, global and local. A global transformation is applicable to the whole image domain, while a local transformation is applicable to only a subset of the image domain.

Transformation type refers to the mathematical form of the spatial mapping used to align two images. Based on the nature of transformation, we can distinguish registration into four classes (see Figure 2.1). Each class in the following contains the ones before it as special cases.

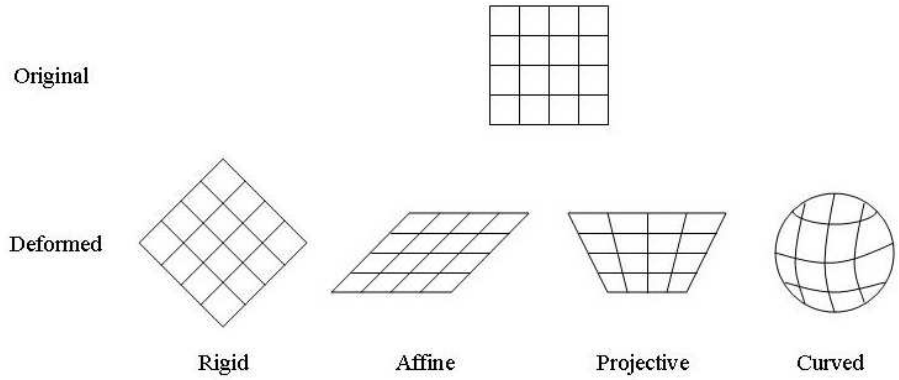

Figure 2.1: Four types of transformations.

Rigid transformations only allow translation and rotation of one image with respect to the other, and thus preserve shapes. This class of registration problems (e.g., [29], [41]) involve computation with six degrees of freedom in three dimensions: three rotation angles and three translation distances. Only a small fraction of

registration problems are of this type. More often, nonrigid transformations with much more degrees of freedom are required for medical registration [13].

Nonrigid transformations contain three subclasses: affine, projective, and curved. Affine transformations take into account scalings and skews. They map parallel lines onto parallel lines, but angles between lines may change. Projective transformations map lines onto lines. They preserve the straightness of lines, and hence, planarity of surfaces. The transformations mentioned till now are linear and global in nature, thus not being able to model local deformations. Curved transformations provide support for local deformations. They map lines onto curves and therefore allow local warping of image features. Many practical registration tasks require estimation of a curved transformation between images.

2.1.2 Applications

As an often encountered problem in medical imaging, registration has evolved independently in various clinical areas, ranging from computer aided diagnosis to image guided surgery, each with a number of unique applications.

To track the difference of a given piece of anatomy over a period of time, as is the case of tumor growth study, or therapy response assessment, series information is collected using the same imaging modality at multiple times, with time scale ranging from hours to years. Since the patient may move with respect to the scanner, motion between images needs to be corrected before the data is analyzed. Also the time scale may be long enough that the imaged object itself has already changed by growth or shrinkage, and therefore deformation between images has to be captured during the data analysis. Monomodal intrasubject registration is used in this situation to realign each image in the series.

To characterize normal versus abnormal anatomical variations, an atlas image, used as a common reference for comparison, is statistically created combining a collection of anatomical information. Since meaningful comparison between subjects and across populations requires the spatial normalization of the images to be compared, monomodal intersubject registration is used to register individual anatomy to the atlas. This type of registration is very useful for atlas based analysis, e.g.,

segmentation. It can be a difficult problem when the boundaries of structures and substructures are poorly defined, the medical image is noisy, or the spatial resolution is limited. A possible solution is first labeling (possibly by hand) the structure of interest in the atlas, then registering the atlas to another image to be segmented. Once the transformation has been computed, labels assigned to regions can simply be applied to corresponding regions in the other image.

To assist diagnosis and improve treatment, complementary information of the patient needs to be collected from different imaging modalities (most often MR, PET, and CT). Since each image modality highlights a specific part of the body, a step of fusion must be applied to combine multimodal images in a more meaningful way so that they can provide an integrated view. In this case, multimodal intrasubject registration is used to fuse the images into one representation, i.e., one coordinate system. For example, radiation therapy for cancers utilizes not only CT scans but also MR or PET data. The former is used for lesion location and dosage calculation, while the contours of the target region are easier to be outlined by the latter. The combination of the two, on which registration is performed, can be assessed more easily and examined more accurately, and thus allows a better determination of the treatment plan for diagnosticians.

When several MR images acquired on different scanners at different institutions need to be registered, multimodal intersubject registration is applied. MR is a special modality since differences between scanners and in acquisition parameters can be such that the contrast characteristics between images substantially vary. So in some sense, MR is not a single modality due to different pulse sequences used in the imaging process.

2.2 Mathematical Formulation

In the previous sections, we have obtained an intuitive impression about medical image registration. Now we give a formal statement of this problem in mathematics.

Mathematically, an image I may be considered as a mapping of points in the image domain, Ω, to intensities in the intensity range $I(\Omega)$. In practice, Ω consists

of discrete elements (2D pixels or 3D voxels), and the intensity typically ranges from 0 to 255 for a medical image encoded at 8 bits. In this thesis, we consider Ω as a continuous domain (a square in 2D and a cube in 3D). This will allow us to apply physically based models (see Chapter 3). Moreover, for simplicity, we scale $I(\Omega)$ to $[0, 1]$. So an image I is a 2D or 3D function:

$$I : \Omega \rightarrow [0, 1],$$

where $\Omega = [0, 1]^d$, $d \in \{2, 3\}$.

We now formally pose the image registration problem. Given two images, a template $A : \Omega_A \rightarrow [0, 1]$ and a target $B : \Omega_B \rightarrow [0, 1]$, the purpose of registration is to determine a spatial transformation

$$\Phi : \Omega_B \rightarrow \Omega_A,$$

such that corresponding points in Ω_A and Ω_B are mapped (see Figure 2.2, data provided courtesy of Dr. H. Farid in the Computer Science Department at Dartmouth College). Once such transformation is obtained, we say that the template image

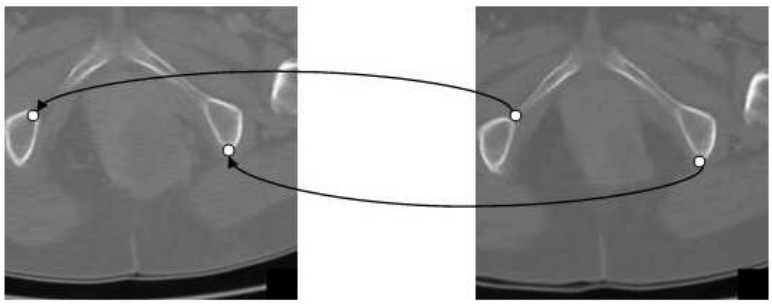

Figure 2.2: Point correspondence between two images of pelvic tumor.

is brought into registration with the target image. The registered image generated from the template consequently becomes $A \circ \Phi : \Omega_B \rightarrow [0, 1]$.

Let $\boldsymbol{x} \in \Omega_B$ and $\boldsymbol{y} \in \Omega_A$ be a corresponding pair in the target and the template, respectively. The difference

$$\Phi(\boldsymbol{x}) - \boldsymbol{y},$$

is called the registration error. Ideally, the transformation Φ is optimal if the registration error is 0. However, in practice, $\boldsymbol{y}$ is unknown and so we cannot compute the registration error. Let's consider monomodal registration and assume that the intensity values are almost the same for the corresponding points in A and B, i.e.,

$$A(\boldsymbol{y}) \approx B(\boldsymbol{x}).$$

Then we can compare $A(\Phi(\boldsymbol{x}))$ and $B(\boldsymbol{x})$ in order to quantify the quality of the spatial transformation Φ.

The image registration problem can now be formulated as an optimization problem:

$$\min_{\Phi} \; D(A \circ \Phi, B), \tag{2.1}$$

where D is a measure of distance between the deformed template and the target. The transformation Φ is determined by minimizing the difference of $A \circ \Phi$ and B. Another possible formulation is:

$$\max_{\Phi} \; S(A \circ \Phi, B),$$

where S is a measure of how similar $A \circ \Phi$ and B are. In this case, Φ is determined by maximizing the similarity between the deformed template and the target. There are several choices for D and S and they often depend on the particular registration problems.

2.2.1 Similarity Measures

If the assumption is made that the images to be registered have similar intensity maps (e.g., monomodal images with identical contrast), an intuitively obvious distance measure is the L_2 norm, i.e., the sum of squared differences (SSD):

$$\text{SSD} = \int_{\Omega} (A(\Phi(\boldsymbol{x})) - B(\boldsymbol{x}))^2 \, d\boldsymbol{x}. \tag{2.2}$$

In this case, SSD will be zero when the images are correctly aligned and will increase quadratically with the registration error. It can be shown that SSD is the optimum measure for images differed only by Gaussian noise [36]. Although the noise present

in medical images is not always Gaussian, SSD is commonly used because of its relatively easy implementation.

Since SSD is highly sensitive to outliers, the sum of absolute differences (SAD) is used as an alternative to reduce the effect of large intensity differences. It is the L_1 norm of the difference of $A \circ \Phi$ and B, defined as

$$\text{SAD} = \int_{\Omega} |A(\Phi(\boldsymbol{x})) - B(\boldsymbol{x})| \, d\boldsymbol{x}. \tag{2.3}$$

In this case, SAD will be zero when the images are correctly aligned and will increase linearly with the registration error. To register images, SAD is minimized. The minimum value corresponds to the smallest total difference of intensities between the target and deformed template.

When the intensity values of corresponding points in two images are not similar, the above measures can not be applied anymore. However, if the intensity maps are linearly related, e.g., monomodal images with different contrast, the correlation coefficient (CC) can be shown to be the ideal similarity measure [36]. It involves the normalized dot product of the difference from the image mean of corresponding intensity values:

$$\text{CC} = \frac{\int_{\Omega}(C(\boldsymbol{x}) - \bar{C})(B(\boldsymbol{x}) - \bar{B}) \, d\boldsymbol{x}}{\sqrt{\int_{\Omega}(C(\boldsymbol{x}) - \bar{C})^2 \, d\boldsymbol{x} \int_{\Omega}(B(\boldsymbol{x}) - \bar{B})^2 \, d\boldsymbol{x}}}.$$

Here C refers to the deformed template $A \circ \Phi$, $\bar{B}$ is the mean of the target image B over Ω, and $\bar{C}$ is the mean of the deformed template C over Ω. To register images, CC is maximized. The maximum value corresponds to the strongest linear relationship of intensities between the target and deformed template.

We have made an assumption on the relationship between image intensity maps for the similarity measures discussed above. If the images to be registered are acquired from different imaging devices, it would require more complex measures to account for the vastly different intensity maps the imaging modalities create. Examples include partitioned intensity uniformity [39], joint entropy [3], and mutual information [22, 37]. In this thesis, we will focus primarily on monomodal registration and so we do not describe these methods here.

2.2.2 Regularization Terms

With no prior knowledge about the desired transformation, the image registration task formulated in (2.1) is an unconstrained optimization problem which turns out to be ill-posed in the sense that multiple solutions could exist (see Figure 2.3).

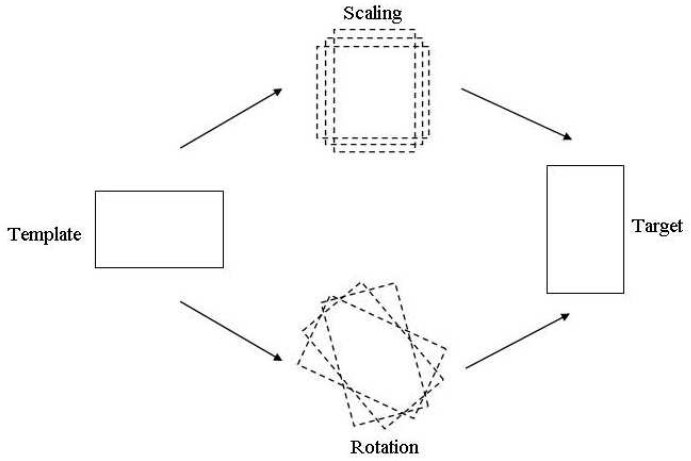

Figure 2.3: A registration example with multiple solutions.

To restrict the solution space, regularization is often used where we specify additional information about the solution by an extra term $R(\Phi)$, called the regularization term. The purpose is to make the corresponding constraint optimization problem a well-posed one:

$$\begin{aligned} &\min_{\Phi} \ D(A \circ \Phi, B), \\ &\text{subject to } R(\Phi) = 0. \end{aligned} \tag{2.4}$$

To simplify notation, we write D as a function of Φ with given A, B. Therefore, the transformation Φ is to minimize the distance measure $D(\Phi)$ while at the same time satisfying some constraint $R(\Phi) = 0$. Equation (2.4) can be rewritten as

$$\min_{\Phi} \ D(\Phi) + \lambda R(\Phi). \tag{2.5}$$

Mathematically, λ is the Lagrange multiplier. In practice, we only treat it as a positive parameter for simplification. The solution of (2.5) is characterized to be the

minimizer of a linear function of the distance measure, which drives the registration as long as the given images are not successfully aligned, and the regularization term, which tends to stop this process when the computed transformation deviates from the desired one.

The desired transformation of an image registration problem depends heavily on the regularization term we impose. A number of different choices exist, each giving the desired transformation unique properties. For example, total variation regularization [25] is used in image denoising and deblurring which can preserve sharp edges. However, more complex regularization terms are required for image registration using physically based models (see Chapter 3).

Chapter 3

Physically Based Models

The region of interest (ROI) in medical images is usually some tissue or organ, such as brain, tumor, and ventricle. If the variation of ROI is caused by the behavior of the corresponding biophysical structures, it is reasonable to acquire the transformation by physically based models described in this chapter. We first introduce the physical analog for image registration, then present required physical principles including conservation laws and constitutive behavior, finally describe related work in physically based registration including elastic models, fluid models, and viscoelastic models.

3.1 Physical Analog

In physically based models, the images to be registered are considered as continuous entities occupying the image domain $\Omega \subset R^d$ ($d \in \{2, 3\}$). Any geometric point in the image corresponds to a material particle in the continuum. Since intensity information is distributed over space, each material particle is assigned an intensity value by its original position in the image. The instantaneous state of the continuum is determined by the position of its material particles. Thus, every state of the continuum, which is associated with a configuration of the material particles, forms a resampling of the intensity values, i.e., a different image. For example, the

template image corresponds to the initial state of the continuum, while the target image corresponds to the final state of the continuum.

To register two images, a body force $\boldsymbol{b}$ is applied on each material particle to drive its movement, and therefore the continuum evolves to the desired state of registration. The body force provides a connection between different states of the deforming continuum and is defined by the information from the images to be registered. It is commonly chosen to be the variation of the distance measure $D(\Phi)$ with respect to the transformation Φ:

$$\boldsymbol{b} = \frac{\delta D(\Phi)}{\delta \Phi},$$

where δ is the variation operator. Here D is considered as a function of the transformation Φ given the template A and target B. It will be made more precise in Section 4.4.1.

The continuum experiences strain under applied forces. Accordingly, the differences between images to be registered are assumed to be caused by such local deformations. Thus, image registration is simulated as a physical deformation process which can be characterized by the following quantities:

$$\begin{aligned}
\varrho &: \Omega \times [0,T] \to R \\
\boldsymbol{b} &: \Omega \times [0,T] \to R^d \\
\boldsymbol{r} &: \Omega \times [0,T] \to R^d \\
\boldsymbol{u} &: \Omega \times [0,T] \to R^d
\end{aligned}$$

where $[0,T]$ is the time interval for simulation, ϱ is the mass density distributed over the continuum, $\boldsymbol{b}$ is the body force that drives the deformation, $\boldsymbol{r}$ is the displacement resulted from the deformation, and $\boldsymbol{u}$ is the velocity which describes the motion of the deformation.

3.2 Basic Principles

In general, the deformation of the continuum is governed by continuum mechanics [32]. We only list here the relevant equations for image registration. For their derivation and other details, we refer the readers to Appendix A.

Continuity equation:

$$\frac{\partial \varrho}{\partial t} + \nabla \cdot (\varrho \boldsymbol{u}) = 0. \tag{3.1}$$

It describes the conservation of mass.

Momentum equations:

$$\varrho \left(\frac{\partial \boldsymbol{u}}{\partial t} + \boldsymbol{u} \cdot \nabla \boldsymbol{u} \right) - \nabla \cdot \boldsymbol{\sigma} - \boldsymbol{b} = 0, \tag{3.2}$$

where $\boldsymbol{\sigma}$ is the Cauchy stress tensor. They describe the conservation of momentum.

Navier-Lame equations for elastic solids:

$$\mu_e \nabla^2 \boldsymbol{r} + (\lambda_e + \mu_e) \nabla (\nabla \cdot \boldsymbol{r}) + \boldsymbol{b} = \varrho \left(\frac{\partial \boldsymbol{u}}{\partial t} + \boldsymbol{u} \cdot \nabla \boldsymbol{u} \right), \tag{3.3}$$

where λ_e, μ_e are the elasticity coefficients. They are derived from the momentum equations with $\boldsymbol{\sigma}$ defined by the Hooke's law.

Navier-Stokes equations for viscous fluids:

$$\mu_v \nabla^2 \boldsymbol{u} + (\lambda_v + \mu_v) \nabla (\nabla \cdot \boldsymbol{u}) + \boldsymbol{b} = \varrho \left(\frac{\partial \boldsymbol{u}}{\partial t} + \boldsymbol{u} \cdot \nabla \boldsymbol{u} \right) + \nabla p. \tag{3.4}$$

where λ_v, μ_v are the viscosity coefficients. They are derived from the momentum equations with $\boldsymbol{\sigma}$ defined by the Stokes and Newtonian fluid assumptions.

Maxwell equations for viscoelastic fluids:

$$\mu_v \nabla^2 \boldsymbol{u} + (\lambda_v + \mu_v) \nabla (\nabla \cdot \boldsymbol{u}) + \nabla \cdot \boldsymbol{\epsilon} + \boldsymbol{b} = \varrho \left(\frac{\partial \boldsymbol{u}}{\partial t} + \boldsymbol{u} \cdot \nabla \boldsymbol{u} \right) + \nabla p. \tag{3.5}$$

where $\boldsymbol{\epsilon}$ is the extra elastic tensor. They are modified from the Navier-Stokes equations with an additional elastic term.

3.3 Related Work

Widely used in image registration, physically based models control the registration process such that it follows physical laws of dynamics. Thus, the regularization term in (2.4) is typically selected to be some energy form. Since Φ is determined by $\boldsymbol{r}$ and λ is positive, (2.4) is equivalent to

$$\min_{\boldsymbol{r}} \ \frac{1}{\lambda} D(\boldsymbol{r}) + R(\boldsymbol{r}), \tag{3.6}$$

3.3.1 Elastic Models

Broit [6] was the first to study nonrigid registration problems using elastic models. His work was extended by Bajcsy et al. [2] and various variational forms [8, 11] were presented later. In general, elastic models are based on linear elasticity and describe local deformations between images to be registered. The central idea is to consider images as isotropic elastic solids and to model the geometric differences between images as an elastic deformation. Accordingly, the regularization term R in (3.6) is chosen to be the elastic potential energy, defined as

$$R(\boldsymbol{r}) = \int_{\Omega} \sum_{i=1}^{d} \sum_{j=1}^{d} \left\{ \frac{\lambda_e}{2} \frac{\partial r_i}{\partial x_i} \frac{\partial r_j}{\partial x_j} + \frac{\mu_e}{4} \left(\frac{\partial r_i}{\partial x_j} + \frac{\partial r_j}{\partial x_i} \right)^2 \right\} d\boldsymbol{x}, \tag{3.7}$$

where $d \in \{2, 3\}$ is the dimension. Initially when the displacement $\boldsymbol{r}$ is zero (i.e., no registration at all), the corresponding value of $R(\boldsymbol{r})$ is the minimum zero, and this value increases with the local deformations developed during the registration process. Therefore, the minimization statement of elastic registration problems involves the determination of a kinematically admissible displacement field $\boldsymbol{r}$ such that some distance measure $D(\boldsymbol{r})$ plus the elastic potential $R(\boldsymbol{r})$ reaches a minimum:

$$\min_{\boldsymbol{r}} \frac{1}{\lambda} D(\boldsymbol{r}) + \int_{\Omega} \sum_{i=1}^{d} \sum_{j=1}^{d} \left\{ \frac{\lambda_e}{2} \frac{\partial r_i}{\partial x_i} \frac{\partial r_j}{\partial x_j} + \frac{\mu_e}{4} \left(\frac{\partial r_i}{\partial x_j} + \frac{\partial r_j}{\partial x_i} \right)^2 \right\} d\boldsymbol{x}. \tag{3.8}$$

It can be minimized by applying optimization schemes such as gradient descent.

An alternative formulation of elastic models can be made by using the equations of motion directly. Since the registration process is simulated as an elastic solid deforming from its natural shape (which corresponds to the template image) to the warped shape (which corresponds to the target image), the dynamics of the system is governed by the Navier-Lame equations given in Section 3.2. In the case of static equilibrium, the acceleration term vanishes and (3.3) is reduced to

$$\mu_e \nabla^2 \boldsymbol{r} + (\lambda_e + \mu_e) \nabla (\nabla \cdot \boldsymbol{r}) + \boldsymbol{b} = 0. \tag{3.9}$$

These are the governing equations for elastic registration, which provide a different form to achieve the desired solution. They simply tell us that the balance between

the external force $\boldsymbol{b}$ applied to the image body and the internal force $\mu_e \nabla^2 \boldsymbol{r} + (\lambda_e + \mu_e)\nabla(\nabla \cdot \boldsymbol{r})$ caused by the deformation $\boldsymbol{r}$ will lead to the desired static equilibrium solution and terminate the registration process. These equations of motion are of elliptic type and may be solved by finite difference and successive overrelaxation (SOR) methods [30].

The equivalence between the equations of motion approach and the minimization statement can be easily demonstrated. Using calculus of variations, one can show that minimizing the objective functional in (3.8) simply gives rise to (3.9). In other words, (3.9) is nothing but the Euler-Lagrange equation of (3.8).

When the image registration process is governed by elastic models, the desired transformation has the virtue of being smooth and preserving the topology of the image. However, elastic models are usually only used for accommodating small deformations because the deformation energy caused by stress increases proportionally with the strength of the deformation. In [10], Christensen et al. provided a largely curved registration case where elastic models would fail (similar to Figure 3.1).

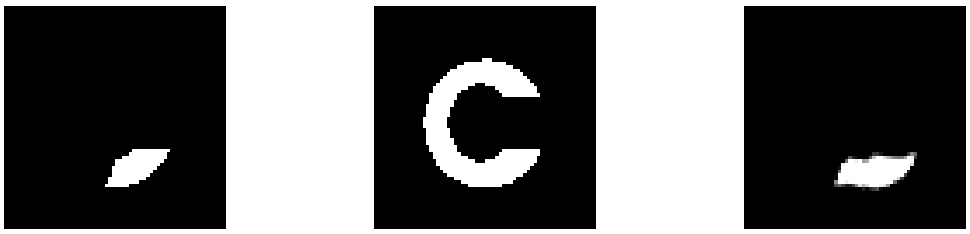

Figure 3.1: A registration example where elastic models would fail: (left) template, (middle) target, (right) deformed template after elastic registration. You start at the template, and try to evolve toward the target, finally get the deformed template.

3.3.2 Fluid Models

An alternative approach based on fluid dynamics has been proposed by Christensen [9]. It models images as Newtonian fluids and simulates the deformation process by

a viscous flow from its original configuration (which corresponds to the template) toward the deformed configuration (which corresponds to the target).

The fluid motion is governed by the Navier-Stokes equations (3.4). For image deformation it is often desirable to include a mass source on a local level, i.e., allow the addition of mass (dilation) or the subtraction of mass (shrinkage) within the control volume. Assuming a source of mass is supplied at a rate of η (negative values correspond to a sink rather than a source) per unit volume, the conservation of mass with a source term consequently becomes

$$\frac{\partial \varrho}{\partial t} + \nabla \cdot (\varrho \boldsymbol{u}) = \eta. \tag{3.10}$$

Similarly, the conservation of momentum with a source term is written as

$$\varrho(\frac{\partial \boldsymbol{u}}{\partial t} + \boldsymbol{u} \cdot \nabla \boldsymbol{u}) + \eta \boldsymbol{u} - \nabla \cdot \boldsymbol{\sigma} - \boldsymbol{b} = 0. \tag{3.11}$$

Substituting the constitutive equation for Newtonian fluids (see Appendix A.2) into (3.11), we obtain the modified Navier-Stokes equations with a mass source:

$$\mu_v \nabla^2 \boldsymbol{u} + (\lambda_v + \mu_v) \nabla (\nabla \cdot \boldsymbol{u}) + \boldsymbol{b} = \varrho(\frac{\partial \boldsymbol{u}}{\partial t} + \boldsymbol{u} \cdot \nabla \boldsymbol{u}) + \eta \boldsymbol{u} + \nabla p. \tag{3.12}$$

A simplified model is obtained [20] for a very low Reynolds number flow where the pressure gradient ∇p and the inertial terms $\varrho(\partial \boldsymbol{u}/\partial t + \boldsymbol{u} \cdot \nabla \boldsymbol{u}) + \eta \boldsymbol{u}$ are neglected, such that (3.12) becomes

$$\mu_v \nabla^2 \boldsymbol{u} + (\lambda_v + \mu_v) \nabla (\nabla \cdot \boldsymbol{u}) + \boldsymbol{b} = 0. \tag{3.13}$$

These are the governing equations for fluid registration, similar to (3.9) except that differentiation is taken on the velocity field $\boldsymbol{u}$ rather than the displacement field $\boldsymbol{r}$. Hence they are solved at each time to compute instantaneous velocity $\boldsymbol{u}$ and update current displacement $\boldsymbol{r}$, which substantially increases the computational cost while maintaining a continuous homeomorphic map. Again, finite difference and SOR methods are often used.

Fluid models are more flexible and can capture large, nonlinear deformations. At the same time the possibility for misregistration increases because of the vast number of degrees of freedom allowed. Also, the reported computational cost can be very expensive [5, 38].

3.3.3 Viscoelastic Models

Since most tissues behave between elastic solids and viscous fluids [24], either an elastic approach or a fluid approach itself may not be accurate enough for registration modeling. We have developed a combined viscoelastic approach [40] which has the property of both elastic solids and viscous fluids to achieve better registration. The basic idea is to model images as viscoelastic fluids and to simulate the deformation process as a flow from the template to the target.

In order to capture the elastic behavior in the transformation, we model the fluid as a viscoelastic fluid. Again assuming very small Reynolds number, we simplify (3.5) and the motion of a viscoelastic fluid is then governed by

$$\mu_v \nabla^2 \boldsymbol{u} + (\lambda_v + \mu_v)\nabla(\nabla \cdot \boldsymbol{u}) + \nabla \cdot \boldsymbol{\epsilon} + \boldsymbol{b} = 0. \tag{3.14}$$

These are the governing equations for viscoelastic registration, modified from (3.13) by introducing an additional elastic term. They allow two images to differ by large deformations like viscous fluid and small deformations like elastic solid. The transformation obtained from (3.14) decreases blurring caused by the fluid terms.

A related approach was proposed by Tang et al. [31]. However, they simplified the linear Maxwell model by direct addition of a fluid part (dashpot) and an elastic part (spring), and solved for each part separately. However for viscoelastic materials, those two parts should be coupled together. Our model applies the coupled constitutive law and thus obtains a more physically realistic analog for medical imaging.

Chapter 4

Inviscid Registration Technique

We present in this chapter an inviscid registration technique expressed in a particle framework. The motivation is to reduce the smearing artifact caused by the viscous terms in fluid models. Under the Eulerian reference frame, we derive the equations of motion which govern the movement of particles. The corresponding variational form for particle registration is also given by using the kinetic energy as the regularization term. To avoid singular mappings, we impose a positive Jacobian requirement on the desired transformation during the particle registration process.

4.1 Motivation

Although fluid models overcome the drawback of elastic models that they only sustain small deformations, the viscous terms included in the fluid equations diffuse the desired transformation, thus naturally resulting in unwanted background movement. Referring to the same registration example shown in Figure 3.1, we inspect the fluid registration results in the following (see Figure 4.1).

This shortcoming of fluid models may affect the registration quality. To avoid undesired background movement, we propose to use an inviscid model. Instead of regarding the image as a fluid continuum with viscous interaction, we simulate the deformation process as a set of free particles moving toward the target image under

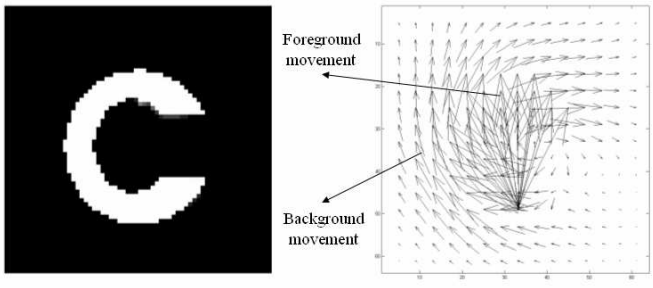

Figure 4.1: Fluid registration results for the same registration example shown before: (left) fluid deformed template, (right) diffused displacement field.

applied forces. It is similar to the case of ideal gas [20] where distances between gas molecules are large enough that internal interaction can be safely ignored and each molecule can be viewed as a particle. In later sections we further show that under the continuous hypothesis this model is closely related to a special inviscid fluid model where the pressure gradient term is dropped.

4.2 Particle Framework

A particle framework for image registration (see Figure 4.2) involves three major parts: an image-to-particle conversion, a particle system simulation, and a particle-to-image reversion. In this framework, the image registration process first converts the template image into an initial particle system, then simulates the evolution of the particle system from its initial state to the final state, and finally reverts the final particle system to the registered image.

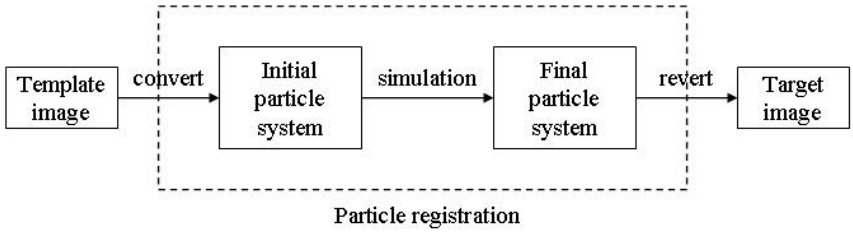

Figure 4.2: Particle framework for image registration.

The image-to-particle conversion describes how to physicalize a given image to its corresponding particle system. Assuming an infinite amount of particles distributed within the image domain, we consider the given image as a particle system associated with a particular distribution of intensity information. Since the particle positions are not necessarily corresponding to image pixels, the intensity information carried on each particle is determined by linear interpolation of neighboring intensity values.

The particle system simulation drives the movement of particles under physical principles. Particles are subject to body force $\boldsymbol{b}$, and the motion of particles is characterized by position $\boldsymbol{x}$, velocity $\boldsymbol{u}$, and displacement $\boldsymbol{r}$. To track every particle from its initial to its final position, conservation laws for mass, momentum, and energy are adopted to govern the evolution of the desired particle system. Each particle is identified on the basis of its final coordinates, which results in the particular choice of the Eulerian reference frame. To make this choice valid for particle framework, we assume the total number of particles is large enough that anytime there exists a particle passing through each observation point. This hypothesis is similar to the continuous assumption stated in Section 3.1.

The particle-to-image reversion describes how to visualize a given particle system to its corresponding image. Since the given particle system distributes particles over space, the intensity information carried on each particle forms a particular distribution over the image domain, and the corresponding image is therefore created by the intensity distribution. As there may be more than one particle within the region of an image pixel, the intensity value of that pixel is determined by weighted interpolation of all intensity values inside. To simplify the computation, we only consider the intensity information carried on the particular particle located at the center of that pixel.

4.2.1 Eulerian Reference Frame

An Eulerian reference frame is used during the image deformation process. To observe the movement of particles, we watch a fixed observation point $\boldsymbol{x}$ in space as time t proceeds. To make this choice of reference frame valid for particle framework,

we assume that there are enough particles moving around. This assumption is similar to the continuous hypothesis in continuum mechanics. Thus, all physical properties such as density, velocity, displacement are considered as functions of $\boldsymbol{x}$ and t. For example, $\boldsymbol{r}(\boldsymbol{x}, t)$ describes the displacement of the particle passing through position $\boldsymbol{x}$ at time t. Accordingly, a particle currently located at position $\boldsymbol{x}$ at time t originated at position $\boldsymbol{x} - \boldsymbol{r}(\boldsymbol{x}, t)$.

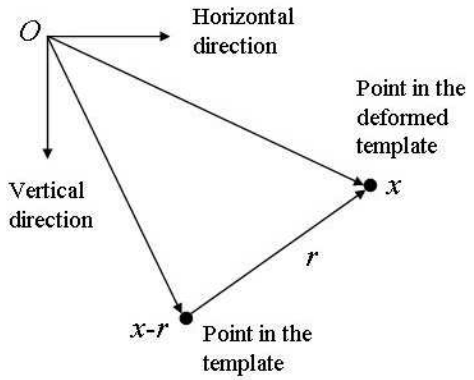

Figure 4.3: Transformation in Eulerian reference frame.

As a consequence, the transformation Φ is applied from the deformed coordinate system back to the original coordinate system, which has the form

$$\Phi : \boldsymbol{x} \rightarrow \boldsymbol{x} - \boldsymbol{r}(\boldsymbol{x}). \tag{4.1}$$

Here $\boldsymbol{x}$ is the point in the deformed template and Φ maps it to its corresponding point in the original template. The offset of the point from its initial position to the final position is described by the displacement vector $\boldsymbol{r}(\boldsymbol{x})$ in Figure 4.3. It is also used to track the deformation of the image over time. Using function notation, (4.1) can be rewritten as

$$\Phi = \boldsymbol{I} - \boldsymbol{r},$$

where $\boldsymbol{I}$ is the identity function.

4.2.2 Material Derivative

From the Eulerian viewpoint, we focus on fixed positions in space at various times and thus lose the ability to easily track the history of a specific particle. To recover

the Lagrangian description of the motion, we need to evaluate the time derivative following a moving particle.

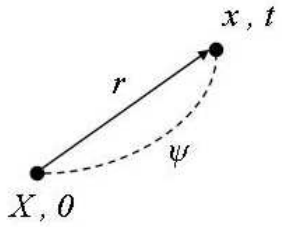

Figure 4.4: Particle trajectory.

Consider a particle initially (at time 0) present in the position $\boldsymbol{X}$ and currently (at time t) occupying the position $\boldsymbol{x}$ (see Figure 4.4). Suppose the trajectory of the particle is described by some function $\Psi(\boldsymbol{X}, t)$, then it satisfies

$$\begin{aligned} \boldsymbol{X} &= \Psi(\boldsymbol{X}, 0), \\ \boldsymbol{x} &= \Psi(\boldsymbol{X}, t). \end{aligned}$$

In addition, the particle displacement is given by the position change:

$$\boldsymbol{r} = \boldsymbol{x} - \boldsymbol{X},$$

and the particle velocity is given by the rate of position change:

$$\boldsymbol{u} = \frac{\partial \Psi}{\partial t}. \tag{4.2}$$

Let f be a physical property associated with the particle, e.g., position, displacement, velocity. It can be represented in two different ways during the motion: Lagrangian variables $f_L(\boldsymbol{X}, t)$ or Eulerian variables $f_E(\boldsymbol{x}, t)$. That is to say

$$f_L(\boldsymbol{X}, t) = f_E(\boldsymbol{x}, t) = f_E(\Psi(\boldsymbol{X}, t), t). \tag{4.3}$$

Differentiating (4.3) with respect to time by applying the chain rules of calculus, we obtain

$$\begin{aligned} \frac{\partial f_L}{\partial t} &= \frac{\partial f_E}{\partial t} + \frac{\partial f_E}{\partial x_1}\frac{\partial \Psi_1}{\partial t} + \frac{\partial f_E}{\partial x_2}\frac{\partial \Psi_2}{\partial t} + \frac{\partial f_E}{\partial x_3}\frac{\partial \Psi_3}{\partial t} \\ &= \frac{\partial f_E}{\partial t} + u_1\frac{\partial f_E}{\partial x_1} + u_2\frac{\partial f_E}{\partial x_2} + u_3\frac{\partial f_E}{\partial x_3}. \end{aligned}$$

The last three additional terms are called convective terms which describe changes due to the fact that the particle changes position. The particular combination on the right hand side has the physical interpretation of the time derivative following a moving particle, which is called the material derivative and often defined by symbol d/dt or D/Dt. In vector notation, it can be written as

$$\frac{d}{dt} = \frac{\partial}{\partial t} + \boldsymbol{u} \cdot \nabla. \tag{4.4}$$

The first term on the right hand side is called the local rate of change, and the second term is called the convective rate of change.

We illustrate the material derivative with one simple example. Take f to be the position vector $\boldsymbol{x}$, hence

$$\begin{aligned} \frac{d\boldsymbol{x}}{dt} &= \frac{\partial \boldsymbol{x}}{\partial t} + \boldsymbol{u} \cdot \nabla \boldsymbol{x} \\ &= 0 + \boldsymbol{u} \\ &= \boldsymbol{u}. \end{aligned}$$

This equation is consistent with our previous definition of velocity and is the Eulerian counterpart of (4.2).

4.3 Governing Equations

Our particle model for image registration includes the differential equations governing the dynamics of the particle system, the boundary conditions, and the initial conditions.

The initial conditions for particle registration is naturally chosen to be

$$\boldsymbol{r}(\boldsymbol{x}, 0) = 0, \ \boldsymbol{u}(\boldsymbol{x}, 0) = 0, \ \text{for any } \boldsymbol{x} \in \Omega. \tag{4.5}$$

To formulate the boundary conditions, we take into account the fact that the objects to be registered usually lie at the center of the image. Therefore, it is reasonable to assume that the image boundary, which is far away from the center, only contains background information (usually black for medical images). Obviously, it remains

constant and needs no registration. Hence zero Dirichlet boundary conditions are used for the particle model which specify the boundary values as follows:

$$\boldsymbol{r}(\boldsymbol{x}, t) = 0,\ \boldsymbol{u}(\boldsymbol{x}, t) = 0,\ \text{for any } \boldsymbol{x} \in \partial\Omega \text{ and } t \in [0, T]. \tag{4.6}$$

These boundary conditions set the velocity and the displacement to be zero at the boundary. Thus, no particles can penetrate the image domain and the system remains static along the boundary.

4.3.1 Compute Velocity

The instantaneous state of a particle is governed by Newton's law of motion. If we assume that there is no internal interaction between particles, the momentum equations (3.2) can be written as

$$\frac{d\boldsymbol{u}}{dt} - \boldsymbol{b} = 0, \tag{4.7}$$

where $\boldsymbol{b}$ is the body force applied to that particle and will be defined later by the information from the template and the target images, $\boldsymbol{u}$ is the consequent velocity which describes the motion of image deformation, and t is the simulation time. The first term of (4.7) represents the force of inertia, i.e., unit mass times the acceleration of a particle.

Expressing d/dt in terms of the material derivative (4.4), we have the following equations which govern the dynamics of the particle system during the image deformation process:

$$\frac{\partial \boldsymbol{u}}{\partial t} + \boldsymbol{u} \cdot \nabla \boldsymbol{u} - \boldsymbol{b} = 0. \tag{4.8}$$

Physically, it means that the body force $\boldsymbol{b}$, which acts upon the whole image domain and drives the registration process, is balanced by the inertial force $d\boldsymbol{u}/dt$ caused by the motion of image deformation.

In contrast with the previously mentioned fluid model (see Section 3.3.2), our particle model is free of viscosity, which can be understood either from the absence of mutual interaction in the particle framework, or from its intimate connection with inviscid fluid models. As the former is obvious, we illustrate the latter here.

A fluid without viscous dissipation is called an inviscid, perfect, or nonviscous fluid [20]. It may or may not be compressible. Referring to the Navier-Stokes equations (3.4) for viscous fluids, "inviscid" simply means $\lambda_v = \mu_v = 0$. Therefore when modeling an inviscid fluid, internal friction is neglected and the stress tensor $\boldsymbol{\sigma}$ is determined solely by the pressure:

$$\boldsymbol{\sigma} = -p\boldsymbol{I}. \tag{4.9}$$

Substituting this stress tensor into (3.2) yields a first-order system of partial differential equations:

$$\varrho(\frac{\partial \boldsymbol{u}}{\partial t} + \boldsymbol{u} \cdot \nabla \boldsymbol{u}) + \nabla p = \boldsymbol{b}, \tag{4.10}$$

which are known as the Euler equations for inviscid fluids. As a simplification of the more realistic Navier-Stokes equations, it is commonly used in gas dynamics. Additional information is needed by invoking the equation of state which relates the pressure p with the density ϱ:

$$p = P(\varrho), \tag{4.11}$$

where P is some algebraic function. For incompressible cases, one can take the density ϱ to be spatially homogenous (in particular, unity). Thus, the pressure p is also a constant over space due to (4.11). Consequently, ϱ and ∇p are both neglected and (4.10) is just reduced to (4.8).

The terms dropped from (3.4) to (4.10) involve second-order derivatives that would make the system parabolic rather than hyperbolic and lead to smooth solutions for all time. Thus, (4.10) has the virtue of allowing discontinuity in solution which turns out to be very useful for image registration problems. Generally, the desired transformation for a registration task may not be smooth. For example, multi-object registration with very close distances and totally different motions requires the desired transformation rapidly varying over a very small common area between the objects. Even for single object registration, the background should not move with the object and thus the interface between the object and the background experiences discontinuous transformation. As a special case of (4.10), (4.8) is good at handling such situations. Therefore, we expect our particle model to be capable of accommodating large deformations yet avoiding the blurring artifact due to fluid viscosity.

4.3.2 Update Displacement

To track the movement of a particle through time, we need to find out the relationship between the velocity $\boldsymbol{u}$ and the displacement $\boldsymbol{r}$. As illustrated in Section 4.2.2, the Eulerian description of velocity is given by

$$\boldsymbol{u} = \frac{d\boldsymbol{x}}{dt}. \tag{4.12}$$

For any particle, the current position $\boldsymbol{x}$ and the displacement $\boldsymbol{r}$ are off by the initial position $\boldsymbol{X}$. Thus, we have

$$\begin{aligned} \boldsymbol{u} &= \frac{d\boldsymbol{X}}{dt} + \frac{d\boldsymbol{r}}{dt} \\ &= 0 + \frac{d\boldsymbol{r}}{dt} \\ &= \frac{d\boldsymbol{r}}{dt}. \end{aligned} \tag{4.13}$$

Using the expression of the material derivative (4.4), (4.13) can be rewritten as

$$\frac{\partial \boldsymbol{r}}{\partial t} + \boldsymbol{u} \cdot \nabla \boldsymbol{r} - \boldsymbol{u} = 0. \tag{4.14}$$

With the computed velocity from (4.8), (4.14) is used to update the current displacement. Thus, our particle model consists of solving (4.8) and (4.14). For ease of future reference, we list them together here:

$$\begin{aligned} \frac{\partial \boldsymbol{u}(\boldsymbol{x},t)}{\partial t} &= \boldsymbol{b}(\boldsymbol{x},t) - \boldsymbol{u}(\boldsymbol{x},t) \cdot \nabla \boldsymbol{u}(\boldsymbol{x},t), \\ \frac{\partial \boldsymbol{r}(\boldsymbol{x},t)}{\partial t} &= \boldsymbol{u}(\boldsymbol{x},t) - \boldsymbol{u}(\boldsymbol{x},t) \cdot \nabla \boldsymbol{r}(\boldsymbol{x},t). \end{aligned} \tag{4.15}$$

However, there are three unknowns: $\boldsymbol{u}$, $\boldsymbol{r}$, and $\boldsymbol{b}$. To close the PDE system, we need a definition of the body force $\boldsymbol{b}$. This can be given by interpreting the particle registration problem into the variational form, which will be shown in Section 4.4.1.

4.4 Variational Form

Similar to elastic registration, we can also formulate particle registration into a minimization problem with the form (3.6). SSD is chosen to be the distance measure

here:

$$D(\boldsymbol{r}) = \int_\Omega \frac{1}{2}(A(\boldsymbol{x} - \boldsymbol{r}(\boldsymbol{x}, t)) - B(\boldsymbol{x}))^2 d\boldsymbol{x}. \tag{4.16}$$

Instead of using the elastic potential as the regularization term in (3.8), we propose a kinetic energy model

$$R(\boldsymbol{r}) = \int_\Omega \frac{1}{2}\boldsymbol{u}^2(\boldsymbol{x}, t) d\boldsymbol{x}, \tag{4.17}$$

where $\boldsymbol{u}^2 = \boldsymbol{u} \cdot \boldsymbol{u}$. Hence at any time t during particle registration, the proposed minimization problem is

$$\min_{\boldsymbol{r}} \frac{1}{\lambda} \int_\Omega \frac{1}{2}(A(\boldsymbol{x} - \boldsymbol{r}(\boldsymbol{x}, t)) - B(\boldsymbol{x}))^2 d\boldsymbol{x} + \int_\Omega \frac{1}{2}\boldsymbol{u}^2(\boldsymbol{x}, t) d\boldsymbol{x}. \tag{4.18}$$

The SSD distance measure in (4.18) drives the registration process, while the kinetic regularization term tends to resist motion. The compromise between the two leads to the minimal motion to register the image pair.

4.4.1 Modified Body Force

The body force $\boldsymbol{b}$ moves particles from the template A to the target B. Aforementioned in Section 3.1, it is defined as the variation of the distance measure $D(\Phi)$ with respect to the transformation Φ :

$$\boldsymbol{b} = \frac{\delta D(\Phi)}{\delta \Phi}, \tag{4.19}$$

where δ is the variation operator. In the Eulerian reference frame, Φ is interpreted as $\boldsymbol{I} - \boldsymbol{r}$ where $\boldsymbol{I}$ is the identity function and $\boldsymbol{r}$ is the displacement function. Therefore, we have

$$\frac{\delta \boldsymbol{r}}{\delta \Phi} = \frac{\delta(\boldsymbol{I} - \Phi)}{\delta \Phi} = -1. \tag{4.20}$$

Substituting (4.20) into (4.19), we obtain

$$\boldsymbol{b} = \frac{\delta D(\boldsymbol{r})}{\delta \boldsymbol{r}} \frac{\delta \boldsymbol{r}}{\delta \Phi} = -\frac{\delta D(\boldsymbol{r})}{\delta \boldsymbol{r}}.$$

It shows that the body force $\boldsymbol{b}$ in the Eulerian reference frame is defined as the negative variation of the distance measure $D(\boldsymbol{r})$. Since $D(\boldsymbol{r})$ is given by the SSD distance measure in (4.16), a straightforward calculation shows

$$\boldsymbol{b}(\boldsymbol{x}, t) = \frac{1}{\lambda}(A(\boldsymbol{x} - \boldsymbol{r}(\boldsymbol{x}, t)) - B(\boldsymbol{x}))\nabla A(\boldsymbol{x} - \boldsymbol{r}(\boldsymbol{x}, t)). \tag{4.21}$$

There are two terms in (4.21), one is the difference term $A(\boldsymbol{x}-\boldsymbol{r}(\boldsymbol{x},t))-B(\boldsymbol{x})$ between the deformed template and the target, the other is the gradient term $\nabla A(\boldsymbol{x}-\boldsymbol{r}(\boldsymbol{x},t))$ of the deformed template. For the purpose of registration, the movement of particles should only slow down when the difference term becomes small, which means the magnitude of $\boldsymbol{b}(\boldsymbol{x},t)$ should only be determined by the difference term. Thus, we normalize the gradient term in the body force definition. We choose $\lambda = \|\nabla A(\boldsymbol{x}-\boldsymbol{r}(\boldsymbol{x}))\|/\alpha$ and (4.21) becomes

$$\boldsymbol{b}(\boldsymbol{x},t) = \alpha(A(\boldsymbol{x}-\boldsymbol{r}(\boldsymbol{x},t))-B(\boldsymbol{x}))\frac{\nabla A(\boldsymbol{x}-\boldsymbol{r}(\boldsymbol{x},t))}{\|\nabla A(\boldsymbol{x}-\boldsymbol{r}(\boldsymbol{x},t))\|}, \tag{4.22}$$

where α is a parameter adjusting the magnitude of the body force. Since the calculation (4.22) involves the gradient operator which is sensitive to noise in the image, we perform Gaussian smoothing [16] on the deformed template prior to the gradient computation. It is achieved by convolving the image intensity distribution with the standard Gaussian distribution (which has a mean of zero and a standard deviation of one). The smoothed image $\tilde{C}$ consequently becomes

$$\tilde{C}(\boldsymbol{x},t) = G(\boldsymbol{x}) * C(\boldsymbol{x},t),$$

where $C(\boldsymbol{x},t)$ refers to the deformed template $A(\boldsymbol{x}-\boldsymbol{r}(\boldsymbol{x},t))$, $G(\boldsymbol{x})$ is the standard Gaussian distribution, and $*$ is the convolution operator. The modified body force is finally expressed as

$$\boldsymbol{b}(\boldsymbol{x},t) = \alpha(C(\boldsymbol{x},t)-B(\boldsymbol{x}))\frac{\nabla \tilde{C}(\boldsymbol{x},t)}{\|\nabla \tilde{C}(\boldsymbol{x},t)\|}. \tag{4.23}$$

Thus equations (4.8), (4.14) and (4.23) constitute a complete PDE system. They are our central equations and will be solved by updating $\boldsymbol{r}$ to realize the registration.

4.4.2 Kinetic Regularization Term

The kinetic regularization term (4.17) tries to minimize the kinetic energy, or equivalently, the motion of deformation while registering the image pair. Therefore, unnecessary motion not driven by the body force is removed. It is consistent with the

particle framework where neighborhood movement is avoided due to the absence of mutual interaction.

It can be shown that the variation of (4.17) is just the inertial force $d\boldsymbol{u}/dt$. We illustrate this with the 1D case. Since the integrand in (4.17) is not explicitly a functional of the displacement function, we need to reformulate it in another way. As stated in Section 4.3, the initial velocity is set to be zero. Thus, we have

$$\begin{aligned} \frac{1}{2}u^2(x,t) &= \frac{1}{2}u^2(x,t) - \frac{1}{2}u^2(x,0) \\ &= \int_0^t d\left(\frac{1}{2}u^2\right). \end{aligned}$$

Here u and x are scaler quantities. Using the chain rule of calculus and taking into account the identity $u = dr/dt$, we further obtain

$$\begin{aligned} \frac{1}{2}u^2(x,t) &= \int_{u(x,0)}^{u(x,t)} u\ du \\ &= \int_0^t \frac{du}{dt} u\ dt \\ &= \int_{r(x,0)}^{r(x,t)} \frac{du}{dt}\ dr. \end{aligned}$$

Therefore, (4.17) can be rewritten as

$$R(r) = \int_\Omega K(r)\ dx, \tag{4.24}$$

where the functional $K(r)$ is given by

$$K(r) = \int_{r(x,0)}^{r(x,t)} \frac{du}{dt}\ dr.$$

Taking the variation of (4.24) simply gives us

$$\frac{\delta R(r)}{\delta r} = \frac{\partial K(r)}{\partial r} = \frac{du}{dt}(x,t). \tag{4.25}$$

Therefore, we conclude that the variation of the kinetic regularization term is equal to the inertial force. Using (4.25), the Euler-Lagrange equation of the minimization problem (4.18) will give the PDE formulation (4.7).

4.5 Regularity Constraint

In the above derivation of particle registration, no collision of particles is allowed anytime during the image deformation process. Otherwise particles will interact with each other, and the absence of mutual interaction no longer holds. Collision happens when two or more particles move to an identical position in space. Mathematically, such situation corresponds to a singular mapping between the image points. Thus we need to enforce a regularity constraint on the transformation to ensure that it is regular.

To avoid collision between particles, we require the transformation to be always one-to-one. That means, different particles will never occupy the same point and collide with each other during the registration process. On the other hand, the violation of this constraint indicates a singular transformation where particles may collide with one another.

A necessary condition for a one-to-one transformation is the positive Jacobian [7]. The Jacobian of the transformation Φ is a function J given by

$$J = \det(\nabla\Phi), \tag{4.26}$$

where det is the determinant operator. To utilize the Jacobian in the Eulerian reference frame, we express Φ in terms of $\boldsymbol{r}$. Therefore, we obtain

$$J = \det(\boldsymbol{I} - \nabla\boldsymbol{r}). \tag{4.27}$$

The regularity constraint for particle registration becomes

$$J(\boldsymbol{x}, t) > 0, \text{ for any } \boldsymbol{x} \in \Omega \text{ and } t \in [0, T]. \tag{4.28}$$

To enforce this regularity constraint, a regridding procedure is used (see Section 5.4).

Chapter 5

Numerical Implementation

In this chapter, we present the numerical implementation of the particle model. The objective PDE system is discretized in space and time using finite difference methods. We also impose a regridding procedure to enforce the regularity constraint, and a multiresolution scheme to reduce the computational cost.

5.1 2D Component Form

Without loss of generality, we consider the image domain Ω to be a 2D square $[0,1]^2$ with x and y referring to each dimension. Consequently, any vector quantity defined over Ω is composed of a horizontal component and a vertical component. We use the notation (b,c) for body force, (u,v) for velocity field, and (r,s) for displacement field. The governing equations (4.15) can now be rewritten in component form:

$$\begin{aligned}
\frac{\partial u}{\partial t} &= b - u\frac{\partial u}{\partial x} - v\frac{\partial u}{\partial y}, \\
\frac{\partial v}{\partial t} &= c - u\frac{\partial v}{\partial x} - v\frac{\partial v}{\partial y}, \\
\frac{\partial r}{\partial t} &= u - u\frac{\partial r}{\partial x} - v\frac{\partial r}{\partial y}, \\
\frac{\partial s}{\partial t} &= v - u\frac{\partial s}{\partial x} - v\frac{\partial s}{\partial y},
\end{aligned} \tag{5.1}$$

with the body force calculated by

$$\begin{aligned} b &= \alpha(C-B)\frac{\frac{\partial \tilde{C}}{\partial x}}{\sqrt{(\frac{\partial \tilde{C}}{\partial x})^2+(\frac{\partial \tilde{C}}{\partial y})^2}}, \\ c &= \alpha(C-B)\frac{\frac{\partial \tilde{C}}{\partial y}}{\sqrt{(\frac{\partial \tilde{C}}{\partial x})^2+(\frac{\partial \tilde{C}}{\partial y})^2}}. \end{aligned}$$

Here, B is the target image, C is the deformed template, and $\tilde{C}$ is the smoothed deformed template.

5.2 Discretization in Space

To observe the movement of particles through space, we discretize the image domain $[0,1]^2$ into a regular grid (see Figure 5.1) with $i_{\max}$ cells in the x direction and $j_{\max}$ cells in the y direction. The size of the grid cell in each dimension is

$$\Delta x = \frac{1}{i_{\max}}, \qquad \Delta y = \frac{1}{j_{\max}}.$$

Numerical values of the unknowns are computed at the cell center:

$$\begin{cases} x_i = \dfrac{\Delta x}{2} + i\Delta x, & i = 0, \ldots, i_{\max}-1, \\ y_j = \dfrac{\Delta y}{2} + j\Delta y, & j = 0, \ldots, j_{\max}-1. \end{cases} \tag{5.2}$$

We approximate the continuous space variables such as intensity, force, velocity, and displacement by discrete space values as follows:

$$\begin{aligned} A_{ij} &: \text{the approximation of the template at } (x_i, y_j), \\ B_{ij} &: \text{the approximation of the target at } (x_i, y_j), \\ C_{ij} &: \text{the approximation of the deformed template at } (x_i, y_j), \\ (b_{ij}, c_{ij}) &: \text{the approximation of the body force at } (x_i, y_j), \\ (u_{ij}, v_{ij}) &: \text{the approximation of the velocity at } (x_i, y_j), \\ (r_{ij}, s_{ij}) &: \text{the approximation of the displacement at } (x_i, y_j). \end{aligned}$$

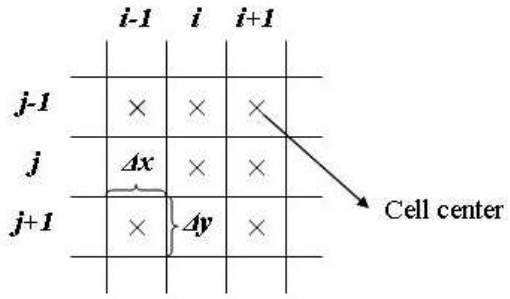

Figure 5.1: Regular grid discretization.

The boundary conditions (4.6) are thus enforced by

$$\begin{cases} b_{ij} = c_{ij} = 0 \\ u_{ij} = v_{ij} = 0 \\ r_{ij} = s_{ij} = 0 \end{cases}, \text{ for } i = 0, i_{\max} - 1, \text{ or } j = 0, j_{\max} - 1.$$

5.2.1 Linear Interpolation

In general, the regular grid imposed on the image domain is chosen to be the pixel lattice. Each cell in the grid becomes an image pixel, and the cell center corresponds to the pixel location. As the image deforms, the particles being tracked at the cell centers may originate from points that do not necessarily correspond to pixel locations (see Figure 5.2). Therefore interpolation is required to compute the approximate intensity values at these points.

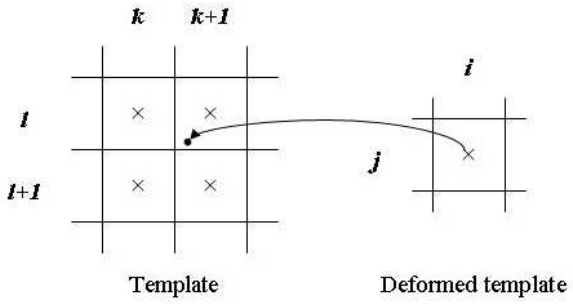

Figure 5.2: Linear interpolation from deformed template to template.

Consider the point (x_i, y_j) in the deformed template C. Since it is mapped back to the point $(x_i - r_{ij}, y_j - s_{ij})$ in the template A, we have

$$C(x_i, y_j) = A(x_i - r_{ij}, y_j - s_{ij}).$$

For an arbitrary point (x, y) in the template A, suppose it is located close to the four cell centers $(x_k, y_l), (x_{k+1}, y_l), (x_k, y_{l+1}), (x_{k+1}, y_{l+1})$. Then its intensity value is approximated by a weighted average of the four nearby intensity values:

$$\begin{aligned} A(x,y) \approx & \frac{(x_{k+1}-x)(y_{l+1}-y)}{(x_{k+1}-x_k)(y_{l+1}-y_l)} A(x_k, y_l) \\ & + \frac{(x_{k+1}-x)(y-y_l)}{(x_{k+1}-x_k)(y_{l+1}-y_l)} A(x_k, y_{l+1}) \\ & + \frac{(x-x_k)(y_{l+1}-y)}{(x_{k+1}-x_k)(y_{l+1}-y_l)} A(x_{k+1}, y_l) \\ & + \frac{(x-x_k)(y-y_l)}{(x_{k+1}-x_k)(y_{l+1}-y_l)} A(x_{k+1}, y_{l+1}). \end{aligned}$$

When substituting $x = x_i - r_{ij}$ and $y = y_j - s_{ij}$, we obtain

$$\begin{aligned} C(x_i, y_j) \approx & \frac{(x_{k+1}-x_i+r_{ij})(y_{l+1}-y_j+s_{ij})}{(x_{k+1}-x_k)(y_{l+1}-y_l)} A(x_k, y_l) \\ & + \frac{(x_{k+1}-x_i+r_{ij})(y_j-y_l-s_{ij})}{(x_{k+1}-x_k)(y_{l+1}-y_l)} A(x_k, y_{l+1}) \\ & + \frac{(x_i-x_k-r_{ij})(y_{l+1}-y_j+s_{ij})}{(x_{k+1}-x_k)(y_{l+1}-y_l)} A(x_{k+1}, y_l) \\ & + \frac{(x_i-x_k-r_{ij})(y_j-y_l-s_{ij})}{(x_{k+1}-x_k)(y_{l+1}-y_l)} A(x_{k+1}, y_{l+1}). \end{aligned}$$

Considering (5.2), the right-hand side becomes

$$\begin{aligned} C_{ij} = & (k+1-i+\frac{r_{ij}}{\Delta x})(l+1-j+\frac{s_{ij}}{\Delta y}) A_{k,l} \\ & + (k+1-i+\frac{r_{ij}}{\Delta x})(j-l-\frac{s_{ij}}{\Delta y}) A_{k,l+1} \\ & + (i-k-\frac{r_{ij}}{\Delta x})(l+1-j+\frac{s_{ij}}{\Delta y}) A_{k+1,l} \\ & + (i-k-\frac{r_{ij}}{\Delta x})(j-l-\frac{s_{ij}}{\Delta y}) A_{k+1,l+1}. \end{aligned}$$

5.2.2 Gaussian Smoothing

A standard Gaussian distribution in 2D has the form

$$G(x,y) = \frac{1}{2\pi\sigma^2} e^{-\frac{x^2+y^2}{2\sigma^2}},$$

where σ is the standard deviation. This function obtains the maximum value at the central point $(0,0)$, and decreases concentrically with the radius $\sqrt{x^2+y^2}$. In theory a Gaussian distribution is nonzero anywhere, however, it effectively approaches zero at points outside three standard deviations from the center. Thus, we truncate the Gaussian distribution to the region $[-3\sigma, 3\sigma]^2$ and approximate its values with a discrete Gaussian kernel.

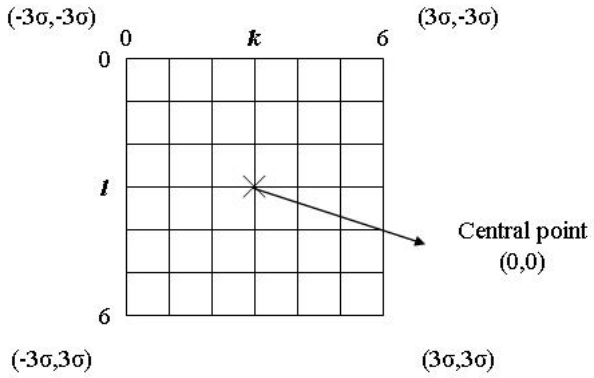

Figure 5.3: Gaussian distribution discretization.

For image smoothing, σ is often chosen as one pixel. The corresponding Gaussian kernel thus has a size of 7×7 as follows:

$$\begin{pmatrix} 0.0000 & 0.0002 & 0.0011 & 0.0018 & 0.0011 & 0.0002 & 0.0000 \\ 0.0002 & 0.0029 & 0.0131 & 0.0215 & 0.0131 & 0.0029 & 0.0002 \\ 0.0011 & 0.0131 & 0.0585 & 0.0965 & 0.0585 & 0.0131 & 0.0011 \\ 0.0018 & 0.0215 & 0.0965 & 0.1592 & 0.0965 & 0.0215 & 0.0018 \\ 0.0011 & 0.0131 & 0.0585 & 0.0965 & 0.0585 & 0.0131 & 0.0011 \\ 0.0002 & 0.0029 & 0.0131 & 0.0215 & 0.0131 & 0.0029 & 0.0002 \\ 0.0000 & 0.0002 & 0.0011 & 0.0018 & 0.0011 & 0.0002 & 0.0000 \end{pmatrix}. \quad (5.3)$$

Each entry in the matrix, identified by discrete indices $k = 0, \ldots, 6$ and $l = 0, \ldots, 6$, locates at the point $(k-3, l-3)$. Therefore, we produce its value by

$$G_{k,l} = \frac{1}{2\pi} e^{-\frac{(k-3)^2+(l-3)^2}{2}}.$$

Consequently, the smoothed deformed template $\tilde{C}$ is computed by the convolution of the Gaussian kernel with the original image C:

$$\tilde{C}_{i,j} = \sum_{k=-3}^{3} \sum_{l=-3}^{3} C_{i+k,j+l} G_{3+k,3+l}.$$

The 2D Gaussian smoothing shown above turns out to be linearly separable; i.e., it can be decomposed into two independent 1D calculations for each component. In this case, the Gaussian kernel in (5.3) reduces to

$$\begin{pmatrix} 0.0044 & 0.0540 & 0.2419 & 0.3989 & 0.2419 & 0.0540 & 0.0044 \end{pmatrix}.$$

The smoothed deformed template is then achieved by first applying a 1D Gaussian smoothing in the horizontal direction, then repeating the process in the vertical direction:

$$\begin{aligned} \hat{C}_{ij} &= \sum_{k=-3}^{3} C_{i+k,j} G_{3+k}, \\ \tilde{C}_{ij} &= \sum_{l=-3}^{3} \hat{C}_{i,j+l} G_{3+l}. \end{aligned}$$

This alternative approach can substantially simplify the computational complexity.

5.2.3 Convective Terms

The discretization of the convective terms needs some care. When discretizing them by central differences, oscillations can occur if the grid spacing $(\Delta x, \Delta y)$ is chosen too coarse [17]. To avoid such instability problems, we replace central differences by upwind differences. Take $\partial u/\partial x$ in (5.1) for example, it is discretized as

$$\left[\frac{\partial u}{\partial x}\right]_{i,j} = \frac{u_r - u_l}{\Delta x} \tag{5.4}$$

where $[\partial u/\partial x]_{i,j}$ represents the approximation of $\partial u/\partial x$ at (x_i, y_j), u_r and u_l are chosen depending on the sign of the convective term. Since the coefficient for $\partial u/\partial x$ is u, we have

$$u_r = \begin{cases} u_{i,j} & \text{if } u_{i,j} > 0, \\ u_{i+1,j} & \text{if } u_{i,j} < 0, \end{cases}$$

and

$$u_l = \begin{cases} u_{i-1,j} & \text{if } u_{i,j} > 0, \\ u_{i,j} & \text{if } u_{i,j} < 0. \end{cases}$$

The above finite difference formulae guarantee the selection of upstream values with respect to the direction of particle motion. We can also rewrite (5.4) as

$$\left[\frac{\partial u}{\partial x}\right]_{i,j} = \frac{u_{i,j} + |u_{i,j}|}{2\Delta x}(u_{i,j} - u_{i-1,j}) + \frac{u_{i,j} - |u_{i,j}|}{2\Delta x}(u_{i+1,j} - u_{i,j}).$$

Similarly, we discretize other convective terms and obtain the following discrete space expressions:

$$\begin{aligned}
\left[\frac{\partial u}{\partial y}\right]_{i,j} &= \frac{v_{i,j} + |v_{i,j}|}{2\Delta y}(u_{i,j} - u_{i,j-1}) + \frac{v_{i,j} - |v_{i,j}|}{2\Delta y}(u_{i,j+1} - u_{i,j}), \\
\left[\frac{\partial v}{\partial x}\right]_{i,j} &= \frac{u_{i,j} + |u_{i,j}|}{2\Delta x}(v_{i,j} - v_{i-1,j}) + \frac{u_{i,j} - |u_{i,j}|}{2\Delta x}(v_{i+1,j} - v_{i,j}), \\
\left[\frac{\partial v}{\partial y}\right]_{i,j} &= \frac{v_{i,j} + |v_{i,j}|}{2\Delta y}(v_{i,j} - v_{i,j-1}) + \frac{v_{i,j} - |v_{i,j}|}{2\Delta y}(v_{i,j+1} - v_{i,j}), \\
\left[\frac{\partial r}{\partial x}\right]_{i,j} &= \frac{u_{i,j} + |u_{i,j}|}{2\Delta x}(r_{i,j} - r_{i-1,j}) + \frac{u_{i,j} - |u_{i,j}|}{2\Delta x}(r_{i+1,j} - r_{i,j}), \\
\left[\frac{\partial r}{\partial y}\right]_{i,j} &= \frac{v_{i,j} + |v_{i,j}|}{2\Delta y}(r_{i,j} - r_{i,j-1}) + \frac{v_{i,j} - |v_{i,j}|}{2\Delta y}(r_{i,j+1} - r_{i,j}), \\
\left[\frac{\partial s}{\partial x}\right]_{i,j} &= \frac{u_{i,j} + |u_{i,j}|}{2\Delta x}(s_{i,j} - s_{i-1,j}) + \frac{u_{i,j} - |u_{i,j}|}{2\Delta x}(s_{i+1,j} - s_{i,j}), \\
\left[\frac{\partial s}{\partial y}\right]_{i,j} &= \frac{v_{i,j} + |v_{i,j}|}{2\Delta y}(s_{i,j} - s_{i,j-1}) + \frac{v_{i,j} - |v_{i,j}|}{2\Delta y}(s_{i,j+1} - s_{i,j}).
\end{aligned}$$

$$\left[\frac{\partial \tilde{C}}{\partial x}\right]_{i,j} = \frac{B_{i,j} - C_{i,j} + |B_{i,j} - C_{i,j}|}{2\Delta x}(\tilde{C}_{i,j} - \tilde{C}_{i-1,j}) + \frac{B_{i,j} - C_{i,j} - |B_{i,j} - C_{i,j}|}{2\Delta x}(\tilde{C}_{i+1,j} - \tilde{C}_{i,j}),$$

$$\left[\frac{\partial \tilde{C}}{\partial y}\right]_{i,j} = \frac{B_{i,j} - C_{i,j} + |B_{i,j} - C_{i,j}|}{2\Delta y}(\tilde{C}_{i,j} - \tilde{C}_{i,j-1}) + \frac{B_{i,j} - C_{i,j} - |B_{i,j} - C_{i,j}|}{2\Delta y}(\tilde{C}_{i,j+1} - \tilde{C}_{i,j}).$$

Since upwind differences are one-sided differences, the order of accuracy is $O(\Delta x, \Delta y)$. In practice, this discretization turns out to be accurate enough for most image registration problems. There are other discretizations available, e.g., Godunov's method, total variation diminishing, if we reformulate the governing equations in conservative forms [21].

5.3 Discretization in Time

To update the movement of particles through time, we discretize the time interval $[0, T]$ into N subintervals:

$$0 = t_0 < t_1 < \ldots < t_n < t_{n+1} < \ldots < t_{N-1} < t_N = T.$$

The stepsize $\Delta t = t_{n+1} - t_n$ is restricted to satisfy the stability conditions (5.5). Initially with given motion, time is incremented by Δt at each timestep $n = 0, \ldots, N$ until the final time T is reached. Thus, the motion at timestep n is known and that at timestep $n + 1$ is to be computed.

We approximate the continuous time variables such as intensity, force, velocity, and displacement by discrete time values as follows:

C^n : the approximation of the deformed template at the timestep n,

(b^n, c^n) : the approximation of the body force at the timestep n,

(u^n, v^n) : the approximation of the velocity at the timestep n,

(r^n, s^n) : the approximation of the displacement at the timestep n.

The initial conditions (4.5) are then enforced by

$$\begin{cases} r^0 = s^0 = 0, \\ u^0 = v^0 = 0. \end{cases}$$

5.3.1 Time Stepping

To discretize the time derivatives, we use Euler explicit method which employs information from one timestep back. For instance, $\partial u/\partial t$ is discretized as

$$\left[\frac{\partial u}{\partial t}\right]^{n+1} = \frac{u^{n+1} - u^n}{\Delta t},$$

where $[\partial u/\partial t]^{n+1}$ represents the approximation of $\partial u/\partial t$ at timestep $n+1$. Meantime, all remaining terms in the same equation are also evaluated at the previous timestep. Therefore, we have

$$u^{n+1} = u^n + \Delta t \left(b^n - u^n \left[\frac{\partial u}{\partial x}\right]^n - v^n \left[\frac{\partial u}{\partial y}\right]^n \right).$$

Similarly, we discretize other time derivatives and obtain the following discrete time expressions:

$$\begin{aligned} v^{n+1} &= v^n + \Delta t \left(c^n - u^n \left[\frac{\partial v}{\partial x}\right]^n - v^n \left[\frac{\partial v}{\partial y}\right]^n \right), \\ r^{n+1} &= r^n + \Delta t \left(u^n - u^n \left[\frac{\partial r}{\partial x}\right]^n - v^n \left[\frac{\partial r}{\partial y}\right]^n \right), \\ s^{n+1} &= u^n + \Delta t \left(v^n - u^n \left[\frac{\partial s}{\partial x}\right]^n - v^n \left[\frac{\partial s}{\partial y}\right]^n \right). \end{aligned}$$

Combining the space discretization described in Section 5.2 gives the fully discrete system in the following:

$$\begin{aligned} b_{ij}^n &= \alpha(C_{ij}^n - B_{ij}) \frac{\left[\frac{\partial \tilde{C}}{\partial x}\right]_{ij}^n}{\sqrt{\left(\left[\frac{\partial \tilde{C}}{\partial x}\right]_{ij}^n\right)^2 + \left(\left[\frac{\partial \tilde{C}}{\partial y}\right]_{ij}^n\right)^2}}, \\ c_{ij}^n &= \alpha(C_{ij}^n - B_{ij}) \frac{\left[\frac{\partial \tilde{C}}{\partial y}\right]_{ij}^n}{\sqrt{\left(\left[\frac{\partial \tilde{C}}{\partial x}\right]_{ij}^n\right)^2 + \left(\left[\frac{\partial \tilde{C}}{\partial y}\right]_{ij}^n\right)^2}}, \end{aligned}$$

$$
\begin{aligned}
u_{ij}^{n+1} &= u_{ij}^{n} + \Delta t \left(b_{ij}^{n} - u_{ij}^{n} \left[\frac{\partial u}{\partial x} \right]_{ij}^{n} - v_{ij}^{n} \left[\frac{\partial u}{\partial y} \right]_{ij}^{n} \right), \\
v_{ij}^{n+1} &= v_{ij}^{n} + \Delta t \left(c_{ij}^{n} - u_{ij}^{n} \left[\frac{\partial v}{\partial x} \right]_{ij}^{n} - v_{ij}^{n} \left[\frac{\partial v}{\partial y} \right]_{ij}^{n} \right), \\
r_{ij}^{n+1} &= r_{ij}^{n} + \Delta t \left(u_{ij}^{n} - u_{ij}^{n} \left[\frac{\partial r}{\partial x} \right]_{ij}^{n} - v_{ij}^{n} \left[\frac{\partial r}{\partial y} \right]_{ij}^{n} \right), \\
s_{ij}^{n+1} &= u_{ij}^{n} + \Delta t \left(v_{ij}^{n} - s_{ij}^{n} \left[\frac{\partial s}{\partial x} \right]_{ij}^{n} - v_{ij}^{n} \left[\frac{\partial s}{\partial y} \right]_{ij}^{n} \right).
\end{aligned}
$$

The time stepping algorithm for particle registration is summarized in Algorithm 1. Note that the regularity constraint discussed in Section 4.5 is imposed from line 10 to line 13, with the details provided later in Section 5.4. This algorithm will stop in two situations. One is the maximum timestep is reached, the other is the deformed template converges to the target.

Algorithm 1 : *Time Stepping*

01. *Initialize* $n \leftarrow 0$, $(u_{i,j}^0, v_{i,j}^0) \leftarrow 0$, *and* $(r_{i,j}^0, s_{i,j}^0) \leftarrow 0$
02. *While* $n < N$, *where* N *is the maximum timestep*
03. *Generate the corresponding deformed template* $C_{i,j}^n$
04. *If* $\max_{i,j} |C_{i,j}^n - B_{i,j}| < \omega$, *where* ω *is the tolerance*
05. *STOP*
06. *EndIf*
07. *Calculate the applied body force* $(b_{i,j}^n, c_{i,j}^n)$
08. *Compute the instantaneous velocity* $(u_{i,j}^{n+1}, v_{i,j}^{n+1})$
09. *Update the current displacement* $(r_{i,j}^{n+1}, s_{i,j}^{n+1})$
10. *Track the resultant Jacobian* $J_{i,j}^{n+1}$
11. *If* $\min_{i,j} J_{i,j}^{n+1} < \varsigma$, *where* ς *is some threshold*
12. *REGRID*
13. *EndIf*
14. *Choose the next stepsize* Δt
15. $n \leftarrow n + 1$
16. *EndWhile*

5.3.2 Stability Conditions

To ensure the stability of numerical computation, we impose the Courant-Friedrichs-Lewy (CFL) conditions [27] on the step size Δt and the cell size $\Delta x \times \Delta y$. They read as follows:

$$|u_{\max}|\Delta t < \Delta x, \qquad |v_{\max}|\Delta t < \Delta y.$$

Here $|u_{\max}|, |v_{\max}|$ refer to the maximum absolute values of the velocity component in each dimension. Under such restrictions, no particles can move further than a cell size in one timestep. In our implementation, we select an adaptive stepsize which satisfies

$$\Delta t = \gamma \min\left(\frac{\Delta x}{|u_{\max}|}, \frac{\Delta y}{|v_{\max}|}\right), \tag{5.5}$$

where $0 < \gamma < 1$ is a safety factor.

5.4 Regridding Procedure

We keep track of the Jacobian through time to ensure a regular transformation. Whenever its minimum value over the grid falls below a certain threshold, a regridding procedure is performed to avoid local singularity. We stop the computation and generate a propagated template equal to the current deformed template. The registration process is restarted by using the propagated template as the new template. The initial displacement is reset to zero and the velocity remains the same.

More precisely, suppose regridding is performed totally M times during the registration process, with each time given by $0 = t_{h_0} < \ldots < t_{h_m} < \ldots < t_{h_M} \leq T$. Let $\{C^{(m)} : 0 \leq m \leq M\}$ represent the sequence of propagated templates corresponding to each regridding. Every propagated template $C^{(m)}$ is deformed in the subinterval $[t_{h_m}, t_{h_{m+1}}]$ to achieve the next propagated template $C^{(m+1)}$ at time $t_{h_{m+1}}$. Thus, we have

$$C^{(m+1)}(\boldsymbol{x}) = C^{(m)}(\boldsymbol{x} - \boldsymbol{r}^{(m)}(\boldsymbol{x}, t_{h_{m+1}})), \tag{5.6}$$

where $\boldsymbol{r}^{(m)}$ is the associated displacement and satisfies

$$\boldsymbol{r}^{(m)}(x, t_{h_m}) = 0.$$

The total displacement with respect to the original template A is consequently obtained by concatenating the displacements associated with each propagated template:

$$\boldsymbol{r}(x,T) = \boldsymbol{r}^{(0)} \circ \cdots \circ \boldsymbol{r}^{(m)} \circ \cdots \circ \boldsymbol{r}^{(M)}(x,T).$$

Therefore, the regridding procedure heuristically decomposes the desired transformation into a sequence of regular transformations between propagated templates. Since the concatenation of one-to-one transformations is again one-to-one, we maintain the positive-Jacobian requirement during the registration process.

5.5 Multiresolution Scheme

To avoid local minimum and speed up computation, a multiresolution scheme is devised for the registration process. The image domain is discretized into multi-level grids with different spacings (see Figure 5.4). We first estimate the global motion at a coarse level, then refine the results with the details provided in the finer levels. The entire procedure is repeated until the full resolution is arrived.

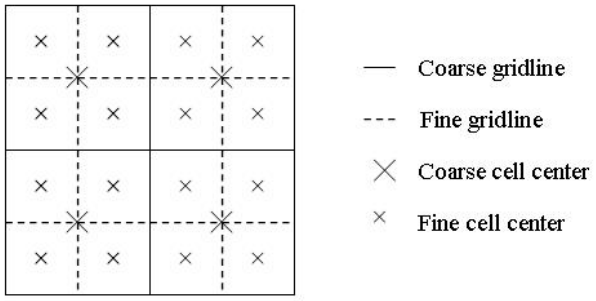

Figure 5.4: Multi-level grid discretization.

In our implementation, a two-level multiresolution is used (see Figure 5.5). However, the same idea can be applied to multiple levels. We identify the coarse level by superscript (c) and the fine level by superscript (f). The given images are first discretized at the fine level by a pixel lattice. Thus, each pixel forms a cell in the fine grid. Then the grid spacing doubles on the coarse level. Accordingly, each cell in the coarse grid is composed of four fine level pixels. The image intensity on

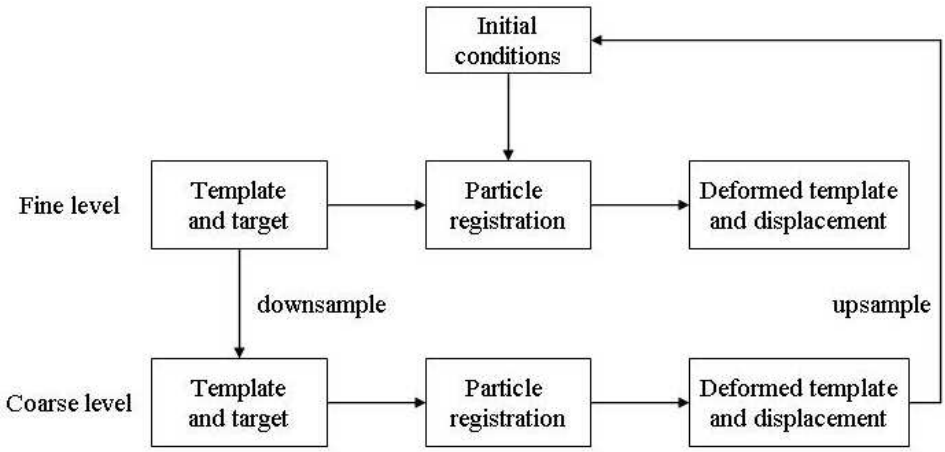

Figure 5.5: Two-level multiresolution scheme.

the coarse level is obtained by the weighted average of the corresponding intensity values on the fine level:

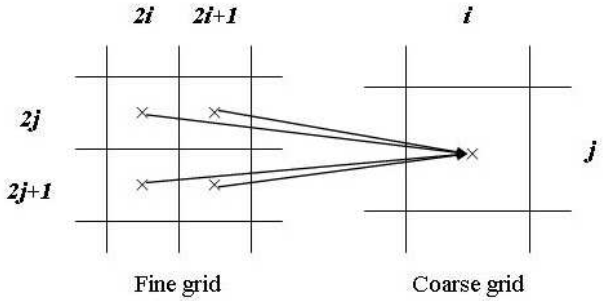

Figure 5.6: Downsampling from fine level to coarse level.

$$\begin{aligned} A^{(c)}_{i,j} &= \frac{1}{4}(A^{(f)}_{2i,2j} + A^{(f)}_{2i,2j+1} + A^{(f)}_{2i+1,2j} + A^{(f)}_{2i+1,2j+1}), \\ B^{(c)}_{i,j} &= \frac{1}{4}(B^{(f)}_{2i,2j} + B^{(f)}_{2i,2j+1} + B^{(f)}_{2i+1,2j} + B^{(f)}_{2i+1,2j+1}). \end{aligned}$$

This process is called downsampling. The registration is then performed on the downsampled images $A^{(c)}, B^{(c)}$. The coarse deformed template $C^{(c)}$ and the displacement field $(r^{(c)}, s^{(c)})$ are upsampled to the fine level:

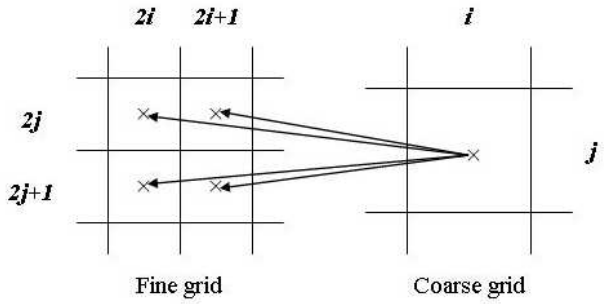

Figure 5.7: Upsampling from coarse level to fine level.

$$\begin{array}{ccccccccc} C^{(c)}_{i,j} & = & C^{(f)}_{2i,2j} & = & C^{(f)}_{2i,2j+1} & = & C^{(f)}_{2i+1,2j} & = & C^{(f)}_{2i+1,2j+1}, \\ r^{(c)}_{i,j} & = & r^{(f)}_{2i,2j} & = & r^{(f)}_{2i,2j+1} & = & r^{(f)}_{2i+1,2j} & = & r^{(f)}_{2i+1,2j+1}, \\ s^{(c)}_{i,j} & = & s^{(f)}_{2i,2j} & = & s^{(f)}_{2i,2j+1} & = & s^{(f)}_{2i+1,2j} & = & s^{(f)}_{2i+1,2j+1}. \end{array}$$

Here we use piecewise constant interpolation. We have also tried piecewise linear interpolation and it does not show any significant benefit. The upsampled deformed template $C^{(f)}$ and displacement field $(r^{(f)}, s^{(f)})$ give a rough estimate of the desired transformation. They are subsequently imposed as initial conditions to effect the registration on the fine level.

Chapter 6

Numerical Results

In this chapter 2D and 3D registration results are presented for a broad range of images, including synthetic cases with known transformations and clinical data in practice. We validate the accuracy and efficiency of our model by means of visual inspection and quantitative measures.

6.1 Overview

Visual inspection involves representing registration in visible forms and studying the result by human eyes. Several sets of images are generated for visual inspection. Firstly, the resulting transformation Φ is applied to the template image A to obtain the deformed template C. It is compared side by side with the target image B. Secondly, a difference image $C - B$ is formed by subtracting the target from the deformed template. If the difference image shows only noise with no structure, the registration is successful; otherwise the images are misregistered. In this thesis, we also apply edge detectors [16] to compare the edge and texture features. If the resulting edge map ∇C is not as clear and sharp as the original one ∇B, that implies a smearing artifact is introduced during registration. Such validation technique is also used in [35]. Finally, the resulting transformation is visualized over the image domain with a displacement map. The translation vector at each

discrete point describes the magnitude and direction of the transformation from the starting position to the end position.

Quantitative measures involves statistical analysis of registration accuracy and algorithm efficiency. To estimate the anatomical differences after registration, we normalize SSD in (2.2) and SAD in (2.3), i.e., the mean of squared differences (MSD) and the mean of absolute differences (MAD). MSD, MAD, as well as CC, are invariant of the size of the image domain, and thus can be used to evaluate the accuracy of different registrations. Besides registration accuracy, algorithm efficiency is also a concern. Since a typical registration algorithm iteratively updates the deformed template to search for a solution closest to the target, the number of iterations as well as the execution times are used to quantify the computational cost.

The proposed model is implemented in C and executed at a desktop PC of P4 2.8G CPU with 1024M memory. The tunable parameters are typically set to $N = 250$, $\alpha = 100$, $\omega = 0.01$, $\varsigma = 0.5$, $\gamma = 0.4$. We also implement the fluid model presented in [10] as a reference. As illustrated in Section 3.3.1, elastic models cannot capture large variations from the template to the target. In the following, we shall compare our model to fluid models only.

6.2 Visual Inspection

We have applied the proposed model to five experiments. The first four are two dimensional and the last one three dimensional. We assume in all experiments that the template and target have roughly the same grey-level values for each constituent structure, and the objects of interest are originally overlapped in the image pair. This requirement can be easily satisfied by a good initial alignment. We also assume that the template and target are padded in all directions by black background (intensity zero). This is due to the fact that the boundary conditions of the velocity and the displacement are set to zero, i.e. the image domain along the boundary has already been mapped. The intensity values are normalized into the range of $[0, 1]$ before registration is performed.

6.2.1 2D Patch to C Experiment

The first experiment depicts the application of our model to 2D synthetic dataset. The purpose of this experiment is to demonstrate the ability of our model to accommodate large curved deformations. We created a pair of synthetic images, consisting of a wedge-shaped template (left) and a "C"-shaped target (right), illustrated in Figure 6.1. These images are similar to those used by [10], but the dimension here is 64×64 pixels. The template was initially aligned with the target so that they overlap.

Figure 6.1: Synthetic images of (left) template, (right) target.

Figure 6.2 shows the progress of deforming a small patch to a longer curved "C" using the particle model. The images from left to right are the propagated templates in a forward time series. Obviously, our model allows the patch template to grow into the "C" target, with the upside of "C" filled by the dilation of the patch. As a result, the image pair are matched completely.

Figure 6.2: Deformation progress from patch to "C".

A vector map of the displacement field for the particle transformation is shown

in Figure 6.3. Since the Eulerian reference frame provides mapping from the target back to the template, each displacement vector finally ends on a regular grid point but originally starts from an irregular location. Compared to the fluid transformation (right), the particle transformation is also largely curved from the small patch to the whole "C". However, the transformation mainly takes place at the patch, and the displacements on the background are mostly zero. This contrasts with the displacement field for the fluid transformation where not only foreground but also background have nonzero displacements.

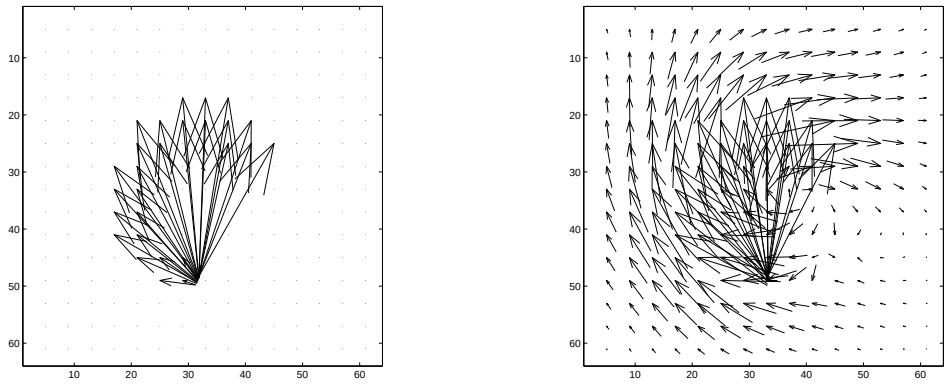

Figure 6.3: Displacement fields for (left) particle transformation, (right) fluid transformation.

6.2.2 2D Square to Circle Experiment

The second experiment illustrates how a nested region deforms from square into circle by the particle transformation. Shown in Figure 6.4 is the square template (left) and the circle target (right) for this experiment. Both images are of size 128×128, with a three-layer nested region at the center. The inner, middle, outer sizes of the nested square are 32, 52, 72 pixels, while the inner, middle, outer diameters of the nested circle are 40, 60, 80 pixels.

Shown in Figure 6.5 are the results for the particle registration. The deformed template (left) is a visual assessment of the registration accuracy. It matches exactly with the nested shape of the circle target. The difference image between the

template and the target (middle) is an estimation of variability before registration. It contains intensity values inside $[-1, 1]$ with positive differences indicated by white, negative differences indicated by black, and zero differences indicated by grey. The difference image between the deformed template and the target (right) is used to check the completeness of registration. It is totally grey (no differences) and thus indicates a complete registration.

Figure 6.4: Synthetic images of (left) template, (right) target

Figure 6.5: Results of (left)deformed template, (middle)difference image between template and target, (right)difference image between deformed template and target.

We compare the displacement fields for the particle transformation and the fluid transformation, as shown in Figure 6.6. The particle transformation (left) deforms the square to circle by smoothing corners and protruding sides only. It is consistent with the fact that differences before registration are only shown in the corner and mid-side regions. However, the fluid transformation (right) results in a spread displacement map which is nonzero almost everywhere. This is due to the neighborhood movement caused by fluid viscosity.

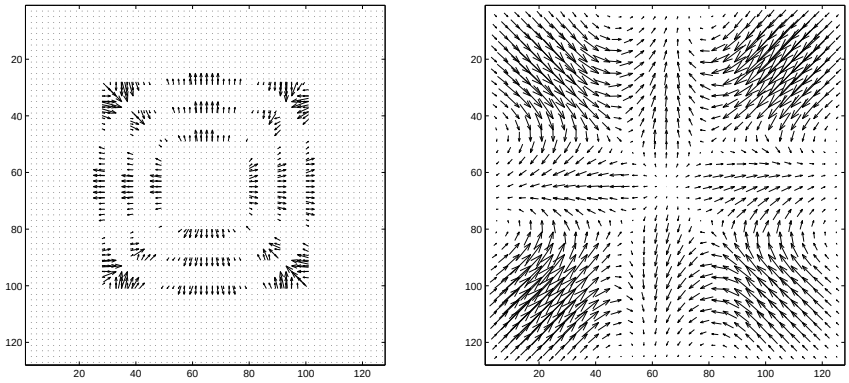

Figure 6.6: Displacement fields of (left) particle transformation, (right) fluid transformation.

6.2.3 2D Segmented Brain Experiment

The third experiment is designed to demonstrate that our model will lead to less blurring artifact than the fluid model. The template (right) and target (left), as illustrated in Figure 6.7, are 256×256, 8-bit, grey-level images of segmented brains. These data were provided courtesy of Dr. H. Farid in the Computer Science Department at the Dartmouth College. The skull part has been stripped and the image pair show the brain region only. Since these images are slices through different subjects, they exhibit obvious variation from each other in limbic system and internal structures. Therefore an amount of nonrigid deformations are required to register the image pair.

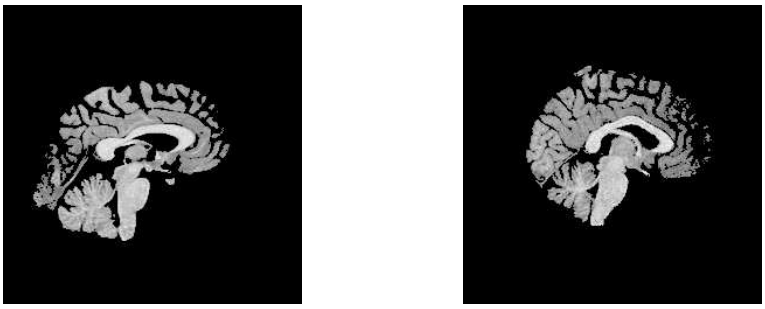

Figure 6.7: Segmented brains of (left) template, (right) target

We study the results given by the particle registration (top) and the fluid registration (bottom) in Figure 6.8. Again, three sets of images are presented for each registration. By inspecting the deformed templates of the two registrations, we find that the fluid model yields a deformed template with blurring in grey cerebral cortex and smearing on white corpus callosum, while the particle model allows different structures to move separately and hence avoids such problems. Since the difference image shows less structure, we conclude that the particle model achieves a better registration (especially in the internal brain region).

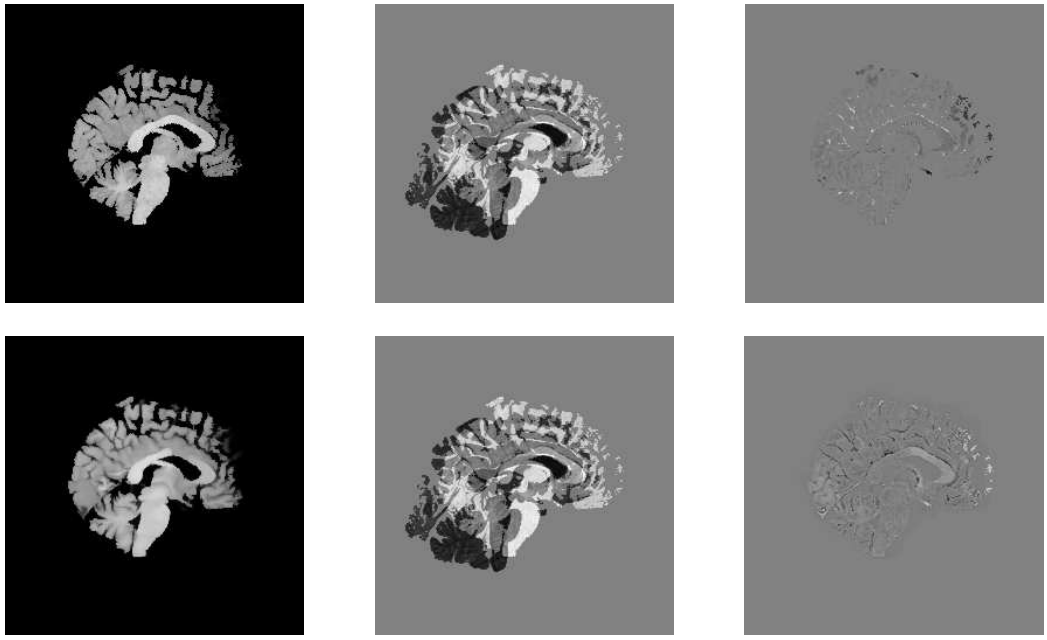

Figure 6.8: Results of (top-left) particle deformed template, (top-middle) difference image before registration, (top-right) difference image after particle registration, (bottom-left) fluid deformed template, (bottom-middle) difference image before registration, (bottom-right) difference image after fluid registration.

To better illustrate that the particle model can achieve a deformed template with sharper edges and clearer texture than the fluid model, we impose sobel edge detector [16] on the target and two transformed templates. As shown in Figure 6.9, the edge maps contain intensity values inside $[0, 1]$ with sharper edges indicated by higher brightness. Note that the edge map of the particle deformed template

is generally brighter than that of the fluid deformed template, indicating that the particle registration is more accurate. In addition, the small circle features inside the cortical region are preserved during the particle registration, while the fluid registration smears texture and blurs edges.

Figure 6.9: Edge maps of (left) target, (middle) particle deformed template, (right) fluid deformed template.

6.2.4 2D Clinical Sagital Experiment

The fourth experiment depicts the application of our model to 2D clinical data. The purpose of this experiment is to demonstrate the ability of our model to capture complex deformations in practice. We applied our model to clinical sagitals as shown in Figure 6.10. The template (left) and target (right) are 256×256, 8-bit, grey-level slices from an MR brain scan. These data are provided courtesy of Dr. J. Orchard in the Computer Science Department at the University of Waterloo. Since the two slices are through the same subject, they contain corresponding constituent structures such as skull, brain, neck, and face. However, the shapes of each constituent structure pair are quite different from each other due to that they are taken from different positions. Consequently the image pair are very difficult to be registered and hence require complex deformations.

The results are shown in Figure 6.11, including the deformed template (left), the difference image between the template and the target (middle), and the difference image between the deformed template and the target (right). Notice that the template and the target greatly differ in the lingua, frontalis, and vertebrae

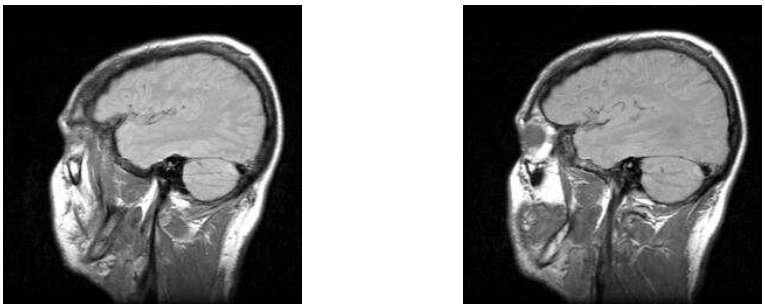

Figure 6.10: Clinical sagitals of (left) template, (right) target

regions. But after registration the differences become very small over the whole brain indicating that the estimated nonrigid transformation is quite accurate. The particle registration has successfully deformed the template toward the target.

Figure 6.11: Results of (left)deformed template, (middle)difference image between template and target, (right)difference image between deformed template and target.

6.2.5 3D Segmented Coronal Experiment

The last experiment depicts the application of our model to 3D clinical data. The purpose of this experiment is to demonstrate that our model can be successfully extended to accommodate 3D complex deformations. The MR volumes used here are stacks of segmented coronals through different subjects which are randomly chosen from IBSR [1]. The skull parts have been stripped and the volumes show

[1]Internet Brain Segmentation Repository. http://www.cma.mgh.harvard.edu/ibsr/

the brain region only. The template and target are 8-bit, grey-level volumes with a dimension of $256 \times 256 \times 63$ at $1mm \times 1mm \times 3mm$. They are symmetrically padded by zeros to produce $256 \times 256 \times 80$ full resolution. Since the borders of the $x - y$ planes have already been mapped, registration is performed in the central square region only and the grid size is chosen to be $160 \times 160 \times 80$. A two-level multiresolution scheme is performed in this experiment to register the template to the target. Thus, the two volumes are downsampled to the coarse level with the grid size of $80 \times 80 \times 40$.

Figure 6.12 shows the results of this experiment. Each row corresponds to a specific coronal slice in the volume (from top to bottom slices 22, 36, 39, 54, and 60, respectively). The columns from left to right correspond to the template, the coarse deformed template, the fine deformed template, and the target, respectively. Notice that the shape variation is accommodated in 3D independent of the slice orientation. This is evident that structures appear and disappear in a fixed slice. For instance, in slice 54 the target differs from the template in two isolated parts from the main structure. As a multiresolution scheme is used for the 3D dataset, the fine deformed templates are obtained based on a good initial alignment given by the coarse deformed templates. Hence they provide more details to approach the targets and are achieved in relatively less time. In fact, the computational cost is reduced from days (without multiresolution) to hours (with multiresolution).

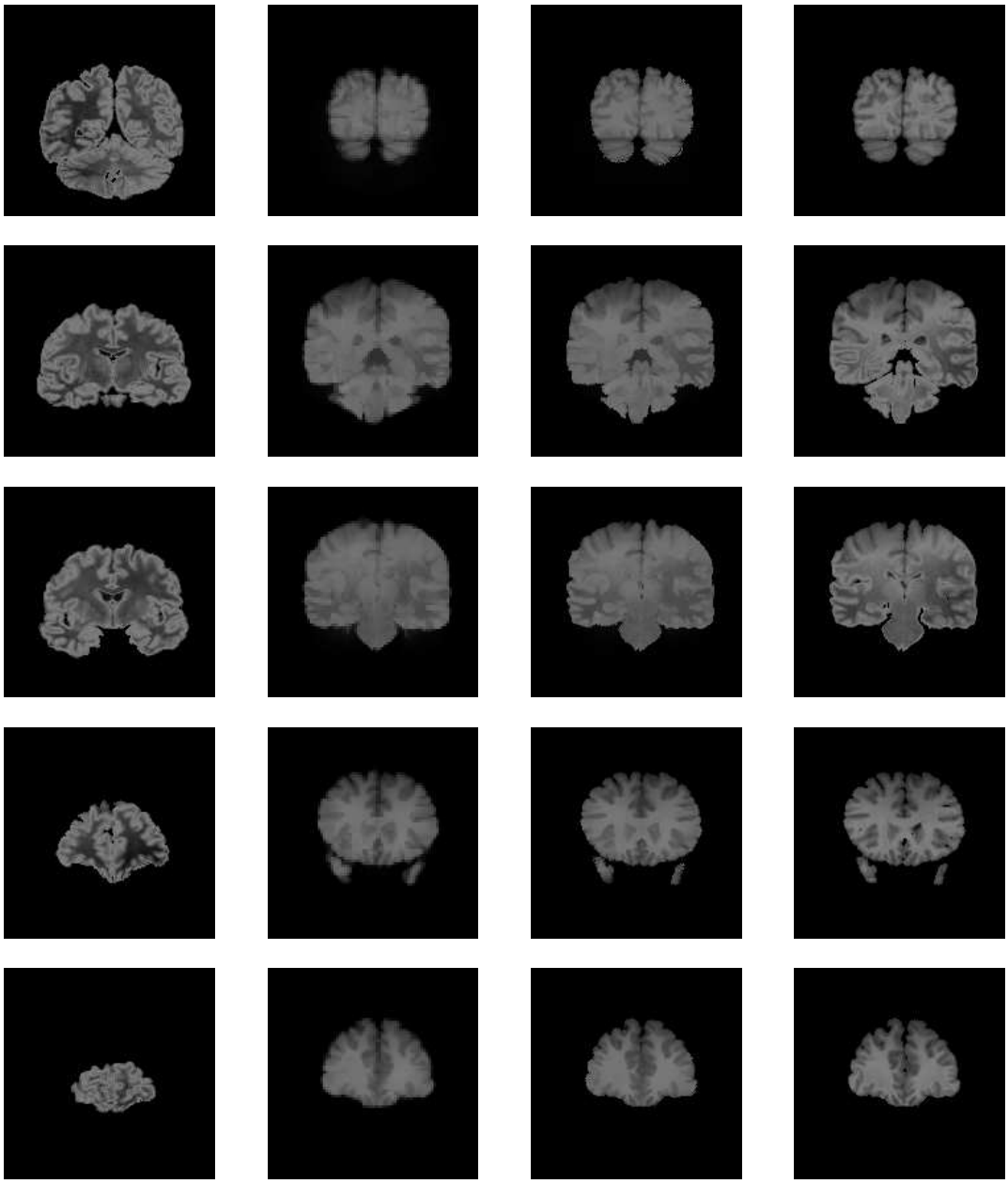

Figure 6.12: Results of (left) template, (middle-left) coarse deformed template, (middle-right) fine deformed template, (right) target.

6.3 Quantitative Measures

We calculate MSD, MAD, CC for each experiment and list them in Tables 6.1 – 6.3, respectively.

Experiment	No registration	Particle registration	Fluid registration
Patch to "C"	0.103760	0.000040	0.000271
Square to Circle	0.010309	0.000002	0.000015
Segmented Brain	0.054380	0.001808	0.002417
Clinical Sagital	0.032019	0.001181	0.001933
Segmented Coronal	0.449359	0.000413	—

Table 6.1: Mean of squared differences for each experiment.

Experiment	No registration	Particle registration	Fluid registration
Patch to "C"	0.103760	0.001305	0.002399
Square to Circle	0.032858	0.000377	0.000735
Segmented Brain	0.090230	0.008101	0.014191
Clinical Sagital	0.100979	0.015249	0.026843
Segmented Coronal	0.047694	0.004282	—

Table 6.2: Mean of absolute differences for each experiment.

Experiment	No registration	Particle registration	Fluid registration
Patch to "C"	0.447277	0.999882	0.998853
Square to Circle	0.940332	0.999990	0.999916
Segmented Brain	0.523169	0.983892	0.977904
Clinical Sagital	0.821038	0.992957	0.988889
Segmented Coronal	0.572913	0.989448	—

Table 6.3: Correlation coefficient for each experiment.

The first column of the above tables gives the name of the experiment described in Section 6.2. The second column shows MSD, MAD, or CC between the template

and the target used in the experiment. The third column shows MSD, MAD, or CC between the deformed template and the target after the particle registration. The last column shows MSD, MAD, or CC between the deformed template and the target after the fluid registration. Note that the fluid registration results for the last experiment are not provided. This is because the last experiment is 3D and executes very slowly for the fluid registration. However, it does not affect much the evaluation of the particle registration.

We can see that MSD and MAD after the particle registration are effectively zero while CC after the particle registration is almost one. It demonstrates that the particle deformed template is quite similar to the target. Comparing with the fluid registration, the particle registration has smaller MSD, smaller MAD, and bigger CC, which indicate a better registration quality.

Experiment	Size	Particle registration	Fluid registration	
			Outer	Inner
Patch to "C"	64×64	214	174	8462
Square to Circle	128×128	119	41	462
Segmented Brain	256×256	98	174	4559
Clinical Sagital	256×256	134	121	4872
Segmented Coronal	$160 \times 160 \times 80$	192	—	

Table 6.4: Number of iterations for each experiment

Experiment	Size	Particle registration	Fluid registration
Patch to "C"	64×64	5	18
Square to Circle	128×128	10	7
Segmented Brain	256×256	34	195
Clinical Sagital	256×256	57	193
Segmented Coronal	$160 \times 160 \times 80$	8238	—

Table 6.5: Execution times in seconds for each experiment

The number of iterations and the execution times for each experiment are summarized in Table 6.4 and Table 6.5. The second column shows the size of the

dataset used in the experiment. The third column shows the number of iterations or the execution time needed for the particle registration. The last column shows the number of iterations or the execution time needed for the fluid registration. Again, the fluid registration results for the last experiment are not provided since it is expected to run for more than a day.

Note that there are two loops of iterations in the fluid registration, outer iterations for maximum timestep and inner iterations for SOR convergence. Each outer iteration involves much more work (tens of inner iterations) than the particle iteration. Thus, the particle registration generally needs a far smaller number of operations and takes less execution times.

To further study the registration process, we keep track of the dynamic MSD for the 2D clinical sagital experiment. Two curves are shown in Figure 6.13, describing the particle registration process (solid line) and the fluid registration process (dotted line), respectively. We can see that the dynamic MSD descends rapidly in the first few seconds during the particle registration process.

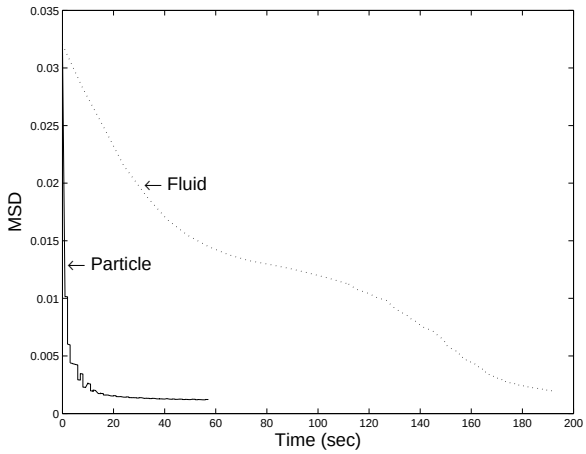

Figure 6.13: Dynamic MSD for 2D clinical sagital experiment during (solid line) particle registration process, (dotted line) fluid registration process.

Chapter 7

Conclusions

Extending existing physically based models, this thesis presents a novel registration technique based on the physical behavior of particles. The central idea is to simulate the registration process as a particle system evolving under applied forces from its initial state (template image) to the final state (target image). As an inviscid model designed for nonrigid registration problems, it is similar to the framework of gas dynamics where distances between gas molecules are large enough that internal friction can be neglected and each molecule is viewed as a free particle. The key features of our model include:

- Not only small linear deformations, but also large nonlinear deformations can be accommodated. Thus, the range of applications is very broad.
- Without mutual interaction, one part of the image moving will not affect other parts. Therefore, the obtained transformation is highly localized such that neighborhood movement is avoided and only motion of objects is captured.
- Due to the absence of fluid viscosity, the blurring effect caused by the viscous terms is eliminated.
- It is very simple to implement and fast to execute.

We have demonstrated the performance of our model on a variety of images including two-dimensional and three-dimensional, synthetic and clinical data. Deformed

images are achieved with sharper edges and clearer texture at less computational cost.

Future efforts will be made in the following aspects. More complicated simulation frameworks can be explored where mutual interaction is added to the particle system. By adjusting the specific form of mutual interaction, the corresponding transformation will possess some global property as well as maintaining certain localization. Also, a mass source can be introduced into physical modeling. The registration process will then take into account a mass equation which controls the shrinkage or dilation of objects. Besides, the particle registration can be performed by minimizing the associated variational form. The current implementation is to solve the Euler-Lagrangian equation whose solution corresponds to a local minimum. Alternatively, one may consider directly applying optimization schemes to the objective functional.

Appendix A

Continuum Mechanics

This appendix reviews some of the fundamental results in continuum mechanics. The conservation laws for mass and momentum are derived, and the constitutive behavior for different materials are presented. We also formulate the governing equations for linear elastic solids, Newtonian fluids, and linear viscoelastic fluids.

A.1 Conservation Laws

The continuum is a closed system in the sense that no material particles penetrate across its boundaries. It is generally assumed that at any time t an arbitrary region Ω_t (in particular, an arbitrary small one) can be selected inside the continuum such that within the region mass, momentum are conserved. Thus, conservation laws can be applied on the control volume Ω_t.

Conservation of Mass

The mass of a continuum occupying a domain is determined by the integral of the density over the domain. Since a constant amount of material particles occupying the control volume Ω_t, we must have for all $t \geq 0$, the rate of change in the mass of a control volume is zero. This is written as

$$\frac{d}{dt}\int_{\Omega_t} \varrho \, d\boldsymbol{x} = 0, \tag{A.1}$$

where ϱ is the mass density distributed over the substance.

Since the surface of the control volume is moving at local velocities, we use the Reynolds transport theorem [20] to move the time differentiation inside the integral. Thus (A.1) becomes

$$\int_{\Omega t} \frac{\partial \varrho}{\partial t}\, d\boldsymbol{x} + \int_{\partial \Omega_t} \varrho \boldsymbol{u} \cdot \boldsymbol{n}\, d\boldsymbol{x} = 0, \tag{A.2}$$

where $\boldsymbol{n}$ is the outward unit normal from $\partial\Omega$. The first term of (A.2) describes the rate of mass change inside the volume Ω, while the second term describes the rate of mass flux across the surface $\partial\Omega$. Applying the divergence theorem [7] to the second term yields

$$\int_{\Omega_t} \left\{ \frac{\partial \varrho}{\partial t} + \nabla \cdot (\varrho \boldsymbol{u}) \right\}\, d\boldsymbol{x} = 0,$$

Noting that the volume integral is arbitrary, this implies that the integral itself vanishes. Hence we obtain the differential form of the mass conservation

$$\frac{\partial \varrho}{\partial t} + \nabla \cdot (\varrho \boldsymbol{u}) = 0. \tag{A.3}$$

This is called the continuity equation.

Conservation of Momentum

The momentum of a continuum occupying a domain is computed by integrating the product of the density with corresponding velocity over the domain. By Newton's second law, we must have for all $t \geq 0$, the rate of change in the linear momentum of a control volume is equal to the sum of the forces acting on the control volume. This is expressed as

$$\frac{d}{dt} \int_{\Omega_t} \varrho \boldsymbol{u}\, d\boldsymbol{x} = \sum \text{ acting forces on } \Omega_t. \tag{A.4}$$

Two types of forces may be distinguished: body forces, which act upon all material particles within the control volume, and surface forces, which act on the boundary surface of the control volume. We let $\boldsymbol{b}$ stand for a body force per unit volume, and

$\boldsymbol{s}$ stand for a surface force per unit area. The resultant force on the control volume consists of the two integrals

$$\sum \text{ acting forces on } \Omega_t = \int_{\Omega_t} \boldsymbol{b}\ d\boldsymbol{x} + \int_{\partial\Omega_t} \boldsymbol{s}\ d\boldsymbol{x}. \tag{A.5}$$

As we know, the surface force $\boldsymbol{s}$ is related to the Cauchy stress tensor $\boldsymbol{\sigma}$ induced within the volume by $\boldsymbol{s} = \boldsymbol{\sigma} \cdot \boldsymbol{n}$. Using this and the divergence theorem to (A.5), together with (A.4), gives

$$\frac{d}{dt} \int_{\Omega_t} \varrho \boldsymbol{u}\ d\boldsymbol{x} = \int_{\Omega_t} (\boldsymbol{b} + \nabla \cdot \boldsymbol{\sigma})\ d\boldsymbol{x}. \tag{A.6}$$

We now apply the Reynolds transport theorem and the divergence theorem componentwise to the left of (A.6). In each dimension this process is similar to what we did for the continuity equation, and the result has the following dimensionless form

$$\frac{d}{dt} \int_{\Omega_t} \varrho \boldsymbol{u}\ d\boldsymbol{x} = \int_{\Omega_t} \left(\frac{\partial \varrho \boldsymbol{u}}{\partial t} + \varrho \boldsymbol{u} \cdot \nabla \boldsymbol{u} + \boldsymbol{u} \nabla \cdot \varrho \boldsymbol{u} \right)\ d\boldsymbol{x}. \tag{A.7}$$

The term on the left of (A.7) describes the time rate of change in the linear momentum of the control volume Ω_t. It is equal to the rate of momentum change inside the volume Ω_t (the first term on the right) plus the rate of momentum flux carried by mass transport across the surface $\partial\Omega_t$ (the other terms on the right). Rearranging (A.7) using the product rule [7] such that (A.3) can be applied, we obtain

$$\frac{d}{dt} \int_{\Omega_t} \varrho \boldsymbol{u}\ d\boldsymbol{x} = \int_{\Omega_t} \varrho \left(\frac{\partial \boldsymbol{u}}{\partial t} + \boldsymbol{u} \cdot \nabla \boldsymbol{u} \right)\ d\boldsymbol{x}. \tag{A.8}$$

Substituting (A.8) into (A.6) yields

$$\int_{\Omega_t} \varrho \left(\frac{\partial \boldsymbol{u}}{\partial t} + \boldsymbol{u} \cdot \nabla \boldsymbol{u} \right)\ d\boldsymbol{x} = \int_{\Omega_t} (\boldsymbol{b} + \nabla \cdot \boldsymbol{\sigma})\ d\boldsymbol{x}. \tag{A.9}$$

Since (A.9) is valid for all choices of control volumes, the differential form of the momentum conservation thus reads

$$\varrho \left(\frac{\partial \boldsymbol{u}}{\partial t} + \boldsymbol{u} \cdot \nabla \boldsymbol{u} \right) - \nabla \cdot \boldsymbol{\sigma} - \boldsymbol{b} = 0. \tag{A.10}$$

These are called the momentum equations. They provide the relationship between the applied body forces and the resulting material deformation. The nature of these equations depends heavily on the model used for the stress tensor $\boldsymbol{\sigma}$, which is discussed later.

A.2 Constitutive Behavior

In order to complete the PDE formulation, we need to specify the constitutive behavior of the material, i.e., a constitutive equation. The constitutive equation connects applied stresses (forces) to resulting strains (deformations). In this section, we describe the constitutive equations for elastic solids, viscous fluids, and viscoelastic fluids.

Elastic Solid

Characterized by resistance to deformation and to changes of volume in a solid, stress is a function of strain. The constitutive relation for linear elastic solids is called the Hooke's law. It states that the amount by which a material body is deformed (i.e., the strain) is linearly related to the force causing the deformation (i.e., the stress). For homogeneous isotropic materials, the linear relation between the stress and the strain reduces to the following

$$\boldsymbol{\sigma} = \lambda_e \mathrm{tr}(\boldsymbol{\epsilon})\boldsymbol{I} + 2\mu_e \boldsymbol{\epsilon}, \tag{A.11}$$

where $\lambda_e, \mu_e > 0$ are the Lame's elastic constants which describe the material properties, $\boldsymbol{\epsilon}$ is the strain tensor, $\boldsymbol{I}$ is the unit tensor, and tr is the trace operator. Assuming small deformations, which is the case of linear elasticity, $\boldsymbol{\epsilon}$ can be given by the Cauchy strain tensor which is defined as

$$\boldsymbol{\epsilon} = \frac{1}{2}\left(\nabla \boldsymbol{r} + (\nabla \boldsymbol{r})^T\right). \tag{A.12}$$

Here $\boldsymbol{r}$ represents the displacement field of the body's configuration (i.e., the difference between the body's configuration and its natural state). Substituting (A.11)

and (A.12) into (A.10), we obtain

$$\mu_e \nabla^2 \boldsymbol{r} + (\lambda_e + \mu_e)\nabla(\nabla \cdot \boldsymbol{r}) + \boldsymbol{b} = \varrho \left(\frac{\partial \boldsymbol{u}}{\partial t} + \boldsymbol{u} \cdot \nabla \boldsymbol{u} \right).$$

They are known as the Navier-Lame equations for elastic solids.

Viscous Fluid

The modeling of fluids separates the Cauchy stress tensor into two contributions:

$$\boldsymbol{\sigma} = \boldsymbol{\tau} - p\boldsymbol{I}, \tag{A.13}$$

where p is the isotropic pressure and $\boldsymbol{\tau}$ is the extra stress tensor representing the forces which the material develops in response to being deformed. Substituting (A.13) into (A.10) results in

$$\nabla \cdot \boldsymbol{\tau} + \boldsymbol{b} = \varrho \left(\frac{\partial \boldsymbol{u}}{\partial t} + \boldsymbol{u} \cdot \nabla \boldsymbol{u} \right) + \nabla p. \tag{A.14}$$

The first term on the right of (A.14) represents the force of inertia, i.e., the density times the acceleration of a fluid particle. To complete the mathematical formulation, we need a constitutive law relating $\boldsymbol{\tau}$ to the motion.

The constitutive relation for a Newtonian fluid [17] obeys the Stokes assumption. As an alternative to Hooke's law used in linear elasticity, it has the property that the extra stress is linear proportional to the rate of strain. Thus $\boldsymbol{\tau}$ is given by

$$\boldsymbol{\tau} = \lambda_v \mathrm{tr}(\boldsymbol{\delta})\boldsymbol{I} + 2\mu_v \boldsymbol{\delta}, \tag{A.15}$$

where λ_v, μ_v are the thermodynamic material constants which describe the fluid viscosity, and $\boldsymbol{\delta}$ is the rate of deformation tensor given by the time derivative of (A.12):

$$\boldsymbol{\delta} = \frac{1}{2}\left(\nabla \boldsymbol{u} + (\nabla \boldsymbol{u})^T \right). \tag{A.16}$$

In contrast with solids which memorize the deformation history, the extra stress within the deformed configuration of fluids is allowed to relax with time.

Substituting (A.15) and (A.16) into (A.14) yields a second-order system of partial differential equations

$$\mu_v \nabla^2 \boldsymbol{u} + (\lambda_v + \mu_v)\nabla(\nabla \cdot \boldsymbol{u}) + \boldsymbol{b} = \varrho \left(\frac{\partial \boldsymbol{u}}{\partial t} + \boldsymbol{u} \cdot \nabla \boldsymbol{u} \right) + \nabla p.$$

They are known as the Navier-Stokes equations for viscous fluids. We define a dimensionless quantity called the Reynolds number:

$$Re = \frac{\varrho_\infty u_\infty L}{\mu_v}, \tag{A.17}$$

where $\varrho_\infty, u_\infty, L$ are the characteristic values of density, velocity, and length, respectively. The Reynolds number represents the relative magnitude of inertial and viscous forces. For $Re \approx 0$ the inertial forces are negligible against the viscous forces (highly viscous fluid), whereas for Re very large the viscous forces can be neglected (inviscid fluid).

Viscoelastic Fluid

In viscoelastic fluids, the stress depends not only on the current motion of the fluid, but also on the history of the motion. If we assume that this dependence is linear, the extra stress tensor given by the Maxwell theory of linear viscoelasticity satisfies

$$\boldsymbol{\tau}_t + \beta \boldsymbol{\tau} = \lambda_v \mathrm{tr}(\boldsymbol{\delta}) \boldsymbol{I} + 2\mu_v \boldsymbol{\delta}, \tag{A.18}$$

where β is a parameter. The quantity $\frac{1}{\beta}$ has the dimension of time and is known as the relaxation time [28]. It is, roughly speaking, a measure of the time for which the fluid remembers the flow history. The competition between the relaxation time and other time scales relevant to the flow determines the behavior of the viscoelastic fluid. If the flow is on a time scale long enough that it quickly loses its memory, the fluid will behave like a Newtonian fluid. On the other hand, when the flow is on a very short time scale with respect to the relaxation time, the memory effect becomes important and the fluid will behave like an elastic solid.

The equations (A.10) and (A.18) for a viscoelastic fluid are coupled together, we have to reformulate the mixed system in a way that tries to separate motion from

constitutive law. Thus, we split the extra stress tensor into an ordinary Newtonian part plus an unknown elastic part:

$$\boldsymbol{\tau} = \lambda_v \mathrm{tr}(\boldsymbol{\delta})\boldsymbol{I} + 2\mu_v \boldsymbol{\delta} + \boldsymbol{\epsilon}. \tag{A.19}$$

This is known as the elastic-viscous stress splitting (EVSS) method [18]. Substituting (A.19) into (A.10), we obtain the Maxwell equations for viscoelastic fluids

$$\mu_v \nabla^2 \boldsymbol{u} + (\lambda_v + \mu_v)\nabla(\nabla \cdot \boldsymbol{u}) + \nabla \cdot \boldsymbol{\epsilon} + \boldsymbol{b} = \varrho \left(\frac{\partial \boldsymbol{u}}{\partial t} + \boldsymbol{u} \cdot \nabla \boldsymbol{u} \right) + \nabla p.$$

They are an extension to the Newtonian fluid case where $\boldsymbol{\epsilon} = 0$ and the momentum equations assume the usual Navier-Stokes form.

Bibliography

[1] Y. Amit. A nonlinear variational problem for image matching. *SIAM Scientific Computing*, 15:207–224, 1994.

[2] R. Bajcsy and S. Kovacic. Multiresolution elastic matching. *Computer Vision, Graphics, and Image Processing*, 46:1–21, 1989.

[3] R. Bansal, L.H. Staib, Z. Chen, A. Rangarajan, J. Knisely, R. Nath, and J.S. Duncan. Entropy-based, multiple-portal-to-3dct registration for prostate radiotherapy using iteratively estimated segmentation. In *Medical Image Computing and Computer-Assisted Intervention*, pages 567–578, 1999.

[4] F.L. Bookstein and W.D.K. Green. Edge information at landmarks in medical images. In *Visualization in Biomedical Computing*, pages 242–258, 1992.

[5] M. Bro-Nielsen and C. Gramkow. Fast fluid registration of medical images. In *Visualization in Biomedical Computing*, pages 267–276, 1996.

[6] C. Broit. *Optimal registration of deformed images*. PhD thesis, University of Pennsylvania, 1981.

[7] R.C. Buck. *Advanced Calculus*. McGraw-Hill, 1978.

[8] G.E. Christensen, S.C. Joshi, and M.I. Miller. Volumetric transformation of brain anatomy. *IEEE Transaction on Medical Imaging*, 16:864–877, 1997.

[9] G.E. Christensen, R.D. Rabbitt, and M.I. Miller. 3d brain mapping using a deformable neuroanatomy. *Physics in Medicine and Biology*, 39:609–618, 1994.

[10] G.E. Christensen, R.D. Rabbitt, and M.I. Miller. Deformable templates using large deformation kinematics. *IEEE Transaction on Image Processing*, 5:1435–1447, 1996.

[11] C. Davatzikos. Spatial transformation and registration of brain images using elastically deformable models. *Computer Vision and Image Understanding*, 66:207–222, 1997.

[12] C. Davatzikos and J.L. Prince. Brain image registration based on curve mapping. In *IEEE Workshop on Biomedical Image Analysis*, pages 245–254, 1994.

[13] B.M. Dawant. Non-rigid registration of medical images: purpose and methods, a short survey. In *IEEE International Symposium on Biomedical Imaging*, pages 465–468, 2002.

[14] A.C. Evans and S. Marrett. Mri-pet correlation in three dimensions using a volume of interest (voi) atlas. *Journal of Cerebral Blood Flow and Metabolism*, 11:A69–A78, 1991.

[15] J.C. Gee, D.R. Haynor, M. Reivich, and R. Bajcsy. Finite element approach to warping of brin images. In *SPIE Medical Imaging*, pages 327–337, 1994.

[16] R. Gonzalez and R. Woods. *Digital Image Processing*. Addison-Wesley, 1992.

[17] M. Griebel, T. Dornseifer, and T. Neunhoeffer. *Numerical Simulation in Fluid Dynamics: A Practical Introduction*. SIAM, 1997.

[18] R. Guenette and M. Fortin. A new mixed finite element method for computing viscoelastic flows. *Journal of Non-Newonian Fluid Mechanics*, 60:27–52, 1999.

[19] A.K. Jain, Y. Zhong, and S. Lakshmanan. Object matching using deformable templates. *IEEE Transactions on Pattern Analysis and Machine Intelligence*, 18:267–277, 1996.

[20] L.D. Landau and E.M. Lifshitz. *Fluid Mechanics*. Pergamon, 1987.

[21] R.J. LeVeque. *Numerical Methods for Conservation Laws*. Birkhauser, 1992.

[22] F. Maes, A. Collignon, D. Vandermeulen, G. Marchal, and P. Suetens. Multimodality image registration by maximization of mutual information. *IEEE Transaction on Medical Imaging*, 16:187–198, 1997.

[23] J. Maintz and M. Viergever. A survey of medical image registration. *Medical Image Analysis*, 2:1–36, 1998.

[24] K. Miller. Finite deformation, linear and nonlinear viscoelastic models of brain tissue mechanical properties. In *Bioengineering*, 1995.

[25] A. Neumaier. Solving ill-conditioned and singular linear systems: a tutorial on regularization. *SIAM Review*, 40, 1998.

[26] C.A. Pelizzari, G.T.Y. Chen, D.R. Spelbring, R.R. Weichselbaum, and C.T. Chen. Accurate three-dimensional registration of ct, pet, and/or mr images of the brain. *Computer Assisted Tomography*, 13:20–26, 1989.

[27] R. Peyret and T. Taylor. *Computational Methods for Fluid Flow*. Springer, 1983.

[28] M. Renardy. *Mathematical Analysis of Viscoelastic Flows*. SIAM, 2000.

[29] A. Roche, X. Pennec, G. Malandain, and N. Ayache. Rigid registration of 3-d ultrasound with mr images: a new approach combining intensity and gradient information. *IEEE Transaction on Medical Imaging*, 20:1038–1049, 2001.

[30] J.C. Strikwerda. *Finite Difference Schemes and Partial Differential Equations*. Wadsworth and Brooks/Cole, 1989.

[31] S. Tang and T. Jiang. Nonrigid registration of medical image by maxwell model of viscoelasticity. In *IEEE International Symposium on Biomedical Imaging: From Nano to Macro*, pages 1443–1446, 2004.

[32] R. Temam and A. Miranville. *Mathematical Modeling in Continuum Mechanics*. Cambridge, 2000.

[33] J. Thirion. Image matching as a diffusion process: an analogy with maxwell's demons. *Medical Image Analysis*, 2:243–260, 1998.

[34] P.M. Thompson and A.W. Toga. A surface-based technique for warping 3-dimensional images of the brain. *IEEE Transaction on Medical Imaging*, 15:1–16, 1996.

[35] B.C. Vemuri, J. Ye, Y. Chen, and C.M. Leonard. Image registration via level-set motion: applications to atlas-based segmentation. *IEEE Transaction on Medical Image Analysis*, 7:1–20, 2003.

[36] P.A. Viola. *Alignment by maximization of mutual information.* PhD thesis, Massachusetts Institute of Technology, 1995.

[37] W.M. Wells, P. Viola, H. Atsumi, S. Nakajima, and R. Kikinis. Multimodal volume registration by maximization of mutual information. *Medical Image Analysis*, 1:35–51, 1996.

[38] G. Wollny and F. Kruggel. Computational cost of nonrigid registration algorithms based on fluid dynamics. *IEEE Transaction on Medical Imaging*, 21:946–952, 2002.

[39] R.P. Woods, J.C. Mazziotta, and S.R. Cherry. Mri-pet registration with automated algorithm. *Computer Assisted Tomography*, 17:536–546, 1993.

[40] Z. Yi and J. Wan. Viscoelastic registration of medical images. Technical Report CS-2005-36, 2005.

[41] L. Zollei, E. Grimson, A. Norbash, and W. Wells. 2d-3d rigid registration of x-ray fluoroscopy and ct images using mutual information and sparsely sampled histogram estimators. In *IEEE Computer Society Conference on Computer Vision and Pattern Recognition*, pages 696–703, 2001.